Multiscale petrographic heterogeneity and their implications for the nanoporous system of the Wufeng-Longmaxi shales in Jiaoshiba area, Southeast China: Response to depositional-diagenetic process.

Article:

Wang, Y orcid.org/0000-0001-9266-1778, Xu, S, Hao, F et al. (5 more authors) (2020) Multiscale petrographic heterogeneity and their implications for the nanoporous system of the Wufeng-Longmaxi shales in Jiaoshiba area, Southeast China: Response to depositional-diagenetic process. GSA Bulletin, 132 (7-8). pp. 1704-1721. ISSN 0016-7606

https://doi.org/10.1130/b35324.1

Multiscale heterogeneity and their implications for the nanoporous system of the Wufeng-Longmaxi shales in Jiaoshiba Area, Southeast China: Response to depositional-diagenetic process

Yuxuan Wang [a], Shang Xu [a]**, Fang Hao [b,] *, Baiqiao Zhang [c],
Zhiguo Shu [c], Qiyang Gou [a], Yangbo Lu [a]

a. Key Laboratory of Tectonics and Petroleum Resources, Ministry of Education, China University of Geosciences, Wuhan 430074, China

b. School of Geosciences, China University of Petroleum, Qingdao 266580, China

c. Research Institute of Petroleum Exploration and Developm ent, Sinopec Jianghan Oilfield Company, Wuhan 430223, China

*Corresponding author: Fang Hao

E-mail address: haofang@cug.edu.cn

Address: School of Geosciences, China University of Petroleum, Changjiangxi Road No.66, Qingdao 266580, China

**Corresponding author: Shang Xu

E-mail address: xushang0222@163.com (S. Xu)

Address: Key Laboratory of Tectonics and Petroleum Resources, Ministry of Education, China University of Geosciences, Lumo Road No.388, Wuhan 430074, China

Abstract

The organic matter-rich shales in Wufeng-Longmaxi Formation are showing a notable heterogeneity characteristic, which significantly controls the mineral composition and organic matter component in the adjacent sections of the shale reservoir. This study combines the multiple scale observation and detailed mineralogical and geochemical analysis to investigate the manifestation, origin, and affection of shale heterogeneity within the equivalent-time stratigraphic framework. The results indicate that polytropic deposition-environment lead to different sediment supplies in the depositional process. After that, these differences among shale sections are magnified through different diagenetic pathways and result in current shale heterogeneity. Section TST is controlled by global glacialism and regional volcanism, leaving an abundance of fine-grained intrabasinal silica and enrichment of organic matter. At diagenesis stage, authigenic quartz aggregates derive from siliceous organisms are spawned. They filled in primary interparticle pores, forming a rigid particle-bracing structure that effectively resisted later compaction and provided enough space for organic matter migrating and occluding. Finally, the production of pores in this migrated organic matter make an essential contribution to the total porosity of shale reservoir. Section EHST is strongly influenced by contour current, which brings about more extrabasinal index and impoverishes organic matter. In diagenesis stage, less siliceous supply could not produce enough authigenic quartz. Therefore, the rigid particle-bracing structure could only preserve in partial place. Primary interparticle pores significantly reduce owing to compaction, leaving less space for later organic matter migrating and occluding. As a result, the total porosity of shale reservoir decline in this section. In a rapid tectonic-uplifting background, section LHST is dominated by a rapid expansion of terrigenous clay minerals and further dilute organic matter.

Ductile clay experiences strong compaction during diagenesis and then occupy most of the primary interparticle space. Rigid particles are wrapped by overwhelmed clays, leading non-existent of the particle-bracing structure. As a result, nanoporous system in shale could not be well preserved.

Keywords

Heterogeneity; Fine-grained Sedimentation; Diagenesis; Nanoporous system; Reservoir quality; Wufeng and Longmaxi shale

1. Introduction

Shale gas is a kind of natural gas that usually contained in shales at the free, absorbing and dissolving state. And it is also one of critical unconventional-gas resources, which is characterized by typical “self-generation and self-storage” pattern (Curtis, 2002; Loucks and Ruppel, 2007; Jarvie et al., 2007; Hao et al., 2013). Although shale reservoir is usually stable and fine-grained compared with sandstone, it still exhibits a strong heterogeneity characteristic (Abouelresh and Slatt, 2012; Hulsey, 2011; Slatt and Rodriguez, 2012). Due to this character, the shale gas production among adjacent sections varies considerably. For example, the characteristic of shale has an extreme difference in the Wufeng-Longmaxi shales of Jiaoshiba gas field (Guo and Zhang, 2014; Guo et al., 2016). Vertically, almost every well shows the section of Wufeng Formation and the adjacent part of Longmaxi Formation have notable higher production than other section. Indeed, shale heterogeneity is one of the key topics of reservoir characterization, which controls the distribution of shale gas accumulation (Li and Jin, 2003; Hammes and Frébourg, 2012; Jiang et al., 2015). Therefore, it is of great significance to figure out the heterogeneity of shales for shale-gas resource evaluation, “sweet spot” prediction and fracturing deployment.

At present, shale heterogeneity has been wildly concerned in shale gas exploration and development. Studies on shale heterogeneity consists of three vital parts: (1) stress anisotropy of shale; (2) pore and fracture system development; (3) heterogeneity modeling (Waleed et al., 2011; Bustin et al.,2012; Loucks et al., 2012; Shebl et al.,2013; Jiang et al., 2015; Zhang et al., 2018). Stress anisotropy analysis could help to predict mud weight and calculate drilling trajectory. Pore and fracture system is the primary storage space of shale gas. They are significantly controlled fracturing parameters and production capacity. Based on the geophysical, geochemical and mineral analysis, heterogeneity modeling combines the shale lithofacies variation, organic matter distribution, rock brittleness, water-bearing, and other vital geological factors to evaluate shale-gas resource potential. However, these studies are mainly focused on the present manifestation of heterogeneity. The origin of heterogeneity, especially its differential evolution process during the depositional and diagenetic stage remains unclear. Furthermore, the inner link of heterogeneity evolution with shale nanoporous system is also not well understood.

Based on observations of the core, thin section, FE-SEM, and nano-CT, this study demonstrates the multiscale heterogeneity of Wufeng-longmaxi shale within the equivalent-time stratigraphic framework. Trough comprehensive study of different depositional environment, diagenetic evolution and hydrocarbon generation process, we analyzed the multiscale heterogeneity in shales of Jiaoshiba Area and discussed how this heterogeneity influenced the nanoporous system of shale reservoir.

2. Geological setting

Since the Yangtze platform developed, it has experienced multiple sedimentary stages and extensively enriched oil and gas resources (Chen et al., 2011; Liu et al., 2013; Fig, 1A). Form the Late Ordovician to Early Silurian, a series of paleo-uplifts and sedimentary centers have formed due to ongoing tectonic uplift around the basin (Fig. 1A). Because of the Guangxian Orogeny intensifying (Chen 2012; Chen et al., 2014), the southeast Cathaysia Block continues advanced, forming the Xuefeng-Qiangzhong foreland uplifts (Li et al., 2010; Chen et al., 2014). The west Chuanzhong uplift is expanding, and the southwest Kangdian oldland is connecting with Qianzhong uplift, forming Dianqiangui Oldland. The Yangtze platform gradually evolved into a siliciclastic-controlled deep shelf basin (Charvet et al., 2010) and Wufeng-Longmaxi black shales widely deposited. Generally, the thickness of Wufeng Formation is 3~5m and it may be thicker in somewhere but no more than 10m (Chen et al., 2015). The Longmaxi Formation is thicker, but the real black shale part only distributed in the bottom side (Fig 1B). It is organic-matter rich and considered to be the main source rocks and major gas reservoir (Hao et al., 2013; Zou et al., 2016).

Sichuan basin is located in the west margin of the Yangtze Platform, which forms a composite basin-range system with orogenic belts around it (Fig. 1A). The Jiaoshiba gas field is located in the east margin of Sichuan Basin, with the total area of approximately 800 km^2. This area has experienced multiple stages of tectonic events, and it is mainly controlled by two groups of faults trending in a NE and NNE direction (Gou, 2013). The major gas-bearing strata is an organic-matter rich shale in the Wufeng Formation (Ordovician) and the Longmaxi Formation (Silurian). It is continuously developed, with an average thickness of about 90 m and moderate burial depth. The underlaying stratum is a nodular limestone bedding of the Jiancaogou Formation and the overlaying part is a grey medium-fine turbidite sandstone. The Guanyinqiao bedding is considered to be an identification of the Ordovician-Silurian boundary (Su et al., 2007). In the study area, it is a dark gray micritic limestone with the thickness of 15~20cm and it does not obviously developed in some wells.

3. Samples and methods

Samples were collected from the three typical drilling cores (JY-A, JY-B, and JY-C) in Jiaoshiba area. All rock samples were analyzed for total organic carbon (TOC) contents, total sulfur (TS) contents, mineral composition, and total porosity. Another samples were selected from them and collected for thin section analysis, field emission-scanning electron microscopy (FE-SEM) and nano-CT analysis. Also, Samples of well JY-A were analyzed for major and trace element concentrations by X-ray fluorescence (XRF) and inductively coupled plasma-mass spectrometer (ICP-MS). Detailed geochemical information was presented by Wang et al., 2019.

Both bulk and clay mineralogical were analyzed using a D/max-2600 X-ray diffractometer (XRD) at Petroleum Geologic Test Center (PGTC) of the Petroleum Exploration and Development Research Institute of Jianghan Oilfield Company, SINOPEC. Powdered samples were placed in copper holders and scanned from 5~90° for whole-rock composition and 3~30° for clay-fraction composition. We used CuKα radiation and a graphite monochromator at 2° min^{-1} with a step width of 0.02°, and its analytical precision was better than 0.02°.

The TOC and TS contents were measured using a CS844-3250 carbon and sulfur analyzer in PGTC. First, each sample was powered into a powder that was finer than the 200-mesh size. Then, we weighed approximately 200 mg of powder and treated it with 10% hydrochloric acid (HCl) at 60°C to remove carbonate. After that, we washed the samples with distilled water to remove the remaining HCl. The samples were then dried and analyzed.

The porosity of 254 samples was measured by helium pycnometry. First samples were dried at 105 °C in a vacuum oven overnight. Then the bulk density of cylindrical plug samples was measured by caliper, and the skeletal density was calculated from the multiple helium expansions. Finally, the porosity can be determined by the differences between the bulk density and skeletal density.

Computerized tomography (CT) scanning is an effective way to characterize the spatial distribution and connectivity of macropores and fractures in shale reservoir (Sun et al., 2016; Ma et al., 2016). Nano-CT analysis experiment was finished at Research Institute of Petroleum Exploration and Development, CNPC, Beijing, using a Nano-CT Xradia scanning device (UltraXRM-L200) produced by Carl Zeiss Company, USA. First, the cylindrical shale sample with a diameter of 1 mm and a length of 0.5 cm was drilled along the vertical bedding direction. Then placed the shale samples horizontally in the A-532-DW Oxford Microscopic Sampling System. After that, samples were cut into miniature cylinders with a diameter of about 65 μm and the length of about 300 μm using a laser beam for Nano-CT scanning. The Nano-CT scanning experiment was at the voltage of 8 kV, the temperature of 20 °C, and the exposure time of 90 s. It supports the maximum resolution of 65 nm.

4. Stratigraphic framework

There has been some stratigraphic study on Wufeng-Longmaxi shale (Hammes and Frébourg, 2012; Chen et al., 2015; Wang et al., 2019). Based on the previous biostratigraphy and sequence stratigraphy study, we reorganized a comprehensive stratigraphic framework of Jiaoshiba area, southeastern Sichuan Basin (Fig. 2). The graptolite biozones, logging data, sequences, and lithofacies are all showing significant variations upward, and they are strongly coupled with each other (Fig. 2). The study interval is divided into 2 third-order sequences. The Wufeng Formation is interpreted as a third order sequence (Sq1), composed of transgressive systems tract (TST 1) and a short highstand systems tract (HST). The Longmaxi Formation is interpreted as another third order sequence (Sq2), which consist of transgressive systems tract (TST 2), early highstand systems tract (EHST) and late highstand systems tract (LHST). Notably, the Guanyinqiao bedding is the main part of HST in Wufeng formation. Because it is very short (~20-50cm) and not easy to identify in many other cores of Jiaoshiba Area. We treat TST 1, HST, and TST 2 for a complete section (TST) at the following discussion (Fig. 2).

Within the sequence stratigraphic framework, the average mineral composition and TOC content of each systems tract differ. The main mineral composition of the shale is quartz, feldspars (K-feldspar and plagioclase), carbonate minerals (calcite and dolomite), clay minerals (illite, chlorite and I/S) and pyrite (Fig. 2). TOC, quartz, and pyrite contents are high in TST and continuous decrease in EHST and LHST whereas clay mineral (illite, chlorite and I/S) contents are opposite (Fig. 3). Feldspar contents (K-feldspar and plagioclase) are relatively high in EHST and very low in TST and LHST (Fig. 3). Carbonate contents in most samples are low, except for some individual peaks (Fig. 3).

5. Results and discussion

5.1 Multiscale heterogeneity in the equivalent-time stratigraphic framework

5.1.1 Centimeter-millimeter scale heterogeneity

The transgressive systems tract (TST) is the major gas-bearing and fracturing section. Six lithofacies has been subdivided (Ma et al., 2016; Wang et al., 2019) based on sedimentary structure, mineralogy, TOC content, and geochemical proxies. Siliceous-rich lithofacies are dominated in this section, including siliceous mudstone (S) and clay-rich siliceous mudstone (CS) (Fig. 3). It also contains some thin carbonate interlayers such as dolomitic-siliceous mudstone (DS) and siliceous-dolomitic mudstone (SD). K-bentonite layers and late pyrite-calcite veins are commonly observed (Fig. 4A). Also, there are abundant graptolite fossils randomly distributed along the bedding plane. It contains a high content of quartz (47.5%) and low content of clay minerals (29.3%). Both feldspar and carbonate mineral are less. The organic matter content is very high, averaging 3.4%. Radiolarians and other siliceous skeletal grains are commonly observed (Fig. 5B, C). Their siliceous outer walls are dissolved, leaving the residue filled with migrated organic matter or calcite (Fig. 5B, C). Besides, the calcareous prominently composed lithofacies is less, which is mainly distributed in other lithofacies in the form of thin interlayers (Fig 3). The carbonate mineral is mainly dolomite and calcite. The granular dolomicrite and quartz are uniformly distributed (Fig. 5D), while the granular dolomite and calcite is mosaically distributed in the clay mineral debris.

The early highstand systems tract (EHST) section is mainly composed of silty stripe shale (Fig. 4B). Silty stripe is densely distributed in the rock core, which is characterized by continuous lenticular or ribbon silty-argillaceous stripe (Fig. 5E). Some abruptly non-invasion top contact between the silty and mud part (Fig. 5F) could also be observed under a microscope. The lenticular intraclasts start to appear, which are mainly composed of clay mineral, fine-grain carbonate mineral and particulate organic matter (Fig. 5F). The number of bentonite beds significantly reduces and is only occasionally 1 to 2 layers. The graptolite is still widely distributed with obvious directionality (Fig. 4B). The average content of quartz is 38.3%. The content of clay mineral, especially chlorite remarkably increases (Fig 3), which is 39.4% on average. The content of organic matter sharply decreases to averagely by 1.9%.

Thick-bedded clay mudstone is dominated in the late highstand systems tract (LHST). Sandy lens could be always observed on the core, and they become bigger upward section. Finally, turbidite sand-stone bedding formed above Longmaxi Formation (Fig. 4C). There are large amounts of relatively coarse grain quartz with crystal shape dispersedly distributed. In some area, there is current bedding formed through scouring (Fig. 5G). The lenticular intraclast appears in quantity in the clay mudstone, which is partly connected and compacted into undulate shape (Fig. 5H). The lenticular intraclast is the aggregation of clay mineral, fine-grain carbonate mineral, and organic matters. The content of clay minerals is quite high, which is 52.0% on average. The average content of the quartz is 32.7%. And the total content of organic matters significantly decreases to 1.2% on average.

5.1.2 Microscale heterogeneity

In section TST, rigid particles like quartz, feldspar, and pyrite are abundant, and most of them are shape-completed. The quartz has two typical shapes. One is relatively bigger with complete crystal shape and smooth edge, which is uniformly distributed (Fig. 6B). Another is smaller with an irregular harbor-shaped edge and radial tips (Fig. 6B). Large amounts of radial quartz are distributed in interparticle space of granular quartz, feldspar and pyrite assemblage (Fig. 6A, B). They form a rigid particle-bracing structure in this section. The organic matter with high content appears in bulk assemblage. It usually fills in the voids of rigid particle skeleton and fossil bodies. The organic-matter pores (OM pores) are also wildly merging (Fig. 6D). In this section, clay minerals are less and distributed inside rigid mineral skeleton or organic matter assemblage (Fig. 6C, D). They are filiform or scaly and have complete intercrystalline pores.

In section EHST, the main rigid particles especially feldspars are significantly increased (Fig. 3), and they also form a particle-bracing structure in some areas (Fig 7A). However, compared with TST, the content of radial quartz remarkably decreases whereas clay minerals notably increase (Fig. 7A, B). In other words, it could not form a complete particle support system without abundant radial quartz. Pyrite framboid assemblages also decrease. The grain size of clay mineral increases to long stripe and scaly shape (Fig 7B). Though the content of it grows, it is not enough to completely warp up the rigid particles (Fig 7B). The content of organic matter decreases, and the organic matter is distributed in the interval between rigid minerals and clay minerals (Fig 7C). The organic pore is well developed (Fig 7C, D). The content of carbonate mineral increases a little bit. The calcite is in irregular shape and cemented distributed (Fig 7D). The dolomite is in particle shape with good crystal shape ankerite along the margin (Fig 7D). Part of carbonate mineral particle has obvious dissolved edge crevice with dissolved pore inside (Fig 7D).

In section LHST, the content of clay minerals significantly increases (Fig 8A). Compared with EHST, the crystal shape rigid minerals such as particle quartz and feldspar are completely wrapped by clay mineral (Fig 8B). The content of quartz, feldspar and other rigid mineral decreases, and even could not contact with each other. It is hard to find large area organic matter assemblage, which is sporadically distributed around the mineral edge supported by single rigid mineral and inside the framboids pyrite particle (Fig 8C, D).

5.1.3 Nanoscale heterogeneity

The three-dimensional Nano-CT technology could describe the spatial distribution and connectivity of macro-pores and micro-fractures in the shale reservoir (Ma et al., 2016; Sun et al., 2016). By Nano-CT analysis, organic matter and pore distribution in different systems tracts are intuitively displayed (Fig. 9A, B). Also, it could further portray the pore connectivity by simulating the information of nanopore and throat system (Fig. 9C). The total volume of each shale three-dimensional data body is 16662.26μm^3. Other detailed pore data obtained by Nano-CT analysis are presented in table 2.

In section TST, the organic matter with high content is evenly distributed. It is well preserved as large plump grains, which connect each other and form irregular columnar assemblages spatially (Fig. 9A1). The shape of pores are irregular, most of them are plump ellipsoid (Fig. 9A2). Almost all of pores distribution correspond well with the organic matter distribution, which may indicate that these pores are OM pores or they are closely related to the evolution of organic matter. Shown as the stick model, pores in this section also has a good conectivity. A large number of pores are interconnected by big throat and a part of them are also linked by additional middlle or small throat (Fig. 9A3). It forms a network structure of the pore-throat system tridimensionally with a wide range of connectivity. As a result, thousands of little pores are recognized as several big pore aggregations, which provide major pore voleum of the sample (Fig. 10A1, A2). Obtained by Nano-CT analysis, the pore volume is 472.68 μm^3 and the porosity is 2.84 %.

In section EHST, compared with TST, the content of organic matter decreases, which has a very uneven distribution (Fig. 9B1). The grain size of organic matter particles remarkably decreases, and their shapes become more angular (Fig. 9B1). Most of the pore distribute correspond well with organic matter (Fig. 9B2). Pore-throat system is also well developed in some partial space. However, these interconnected pore-throat system is much smaller than section TST. They are dispersedly distributed and do not connect with each other (Fig. 9B3). The separate pore number is obviously increased than section TST in every pore diameter interval (Fig. 10B1), whereas total pore volume is decreased into 444.03 μm^3 and the porosity is 2.66 %. (Fig. 10B2).

In section LHST, the OM particles are re-evenly distributed. Most of them are isolating distribution and preserved as small flattened flakes (Fig. 9C1). Pore development is similar to organic matter, and they usually show an oblate shape (Fig. 9C2). Lots of pores are isolated, they are not conneted to any other pores. Other pore-throat systems are small scale. They only connected by a small throat with two adjacent pores (Fig. 9C3). Notably, pore number experiences a significant improvement (Fig. 10C1). The pore size distribution is mainly between 0.1~0.5 μm. Total pore volume decrease to 377.47 μm^3 and the porosity is 2.26 %. (Fig. 10C2).

5.2 Sedimentation controls the primary composition of minerals and organic matter

The organic-rich shale in Wufeng and Longmaxi formation has experienced a turbulent depositional period. The interactions of the global and regional scale geological events control the depositional process of this set of shales (Algeo et al., 2016; Wang et al., 2019), leading a variation of minerals and organic matter composition in the shales of different systems tracts. From the global scale, the Wufeng and Longmaxi formations contains the Ordovician-Silurian global mass extinction boundary (Rong 2006; Fan et al., 2011), worldwide sharply eustatic sea level (Haq and Schutter, 2008) and the grand Hirnantian ice stage (Algeo et al., 2016; Liu et al., 2017). From the regional scale, the continuously tectonic uplifting resulted from the Guangxian Orogeny (Chen et al., 2014), multi-stage and high-intensity volcanism (Su et al., 2007), contour current (Schieber, 1994, 2010; Lu et al., 2017), and the limited-area turbidity currents are also wildly influenced the depositional process of shales in different systems tract.

5.2.1 TST

As the geochemical redox proxies (C-S-Fe relationship, Mo-U convariation, and C_{org}/P-Th/U diagram) displayed in f igures 11, benthic redox condition has experienced a tremendous change from the bottom TST to the top LHST. It reveals that the environment of section TST is anoxic in most of the time (Tribovillard et al., 2006; Algeo and Rowe, 2012). Also, high-content of Si_{xs} indicate that the marine primary productivity keeps a high level (Turgeon and Brumsack, 2006; Ross and Bustin, 2009, Fig. 13B). Meanwhile low Al_2O_3 content represents a low terrigeneous input (Fishman et al., 2015, Fig. 13C). At this period, the Jiaoshiba area was located in the middle part of the sags near the Sichuan Basin (Fig. 1A). It is far from the terrestrial sources with a low sedimentary rate, causing the limitation of extrabasinal minerals like quartz, feldspars and clay minerals. Conversely, the intrabasinal radiolarian, sponge spicules and other siliceous skeleton creatures are commonly observed (Fig. 4B, C). Near the Ordovician-Silurian boundary, the global climate was gradually warming up (Algeo et al., 2016). The rapidly melting of the Hirnantian ice sheet causes the worldwide sea level rise and results in the extensive transgression of South China (Haq and Schutter, 2008). The glacier melting water brings large amounts of nutrients which promotes the growth of primary productivity. In the meantime, the organic matter is well preserved due to the severe hypoxia in the transgression systems tract, especially in the condensed section near the maximum flooding surface (Yan et al., 2015; Wang et al., 2019). There are densely distributed bentonite layers (Fig 4A) in this section, which represent a relatively high frequency and intensity volcanism during the depositional period (Su et al., 2009; Liu et al., 2016). On the one hand, the nutrients from falling volcanic ash contribute to the explosive growth of marine surface primary productivity (Duggen et al., 2007; Langmann et al., 2010). On the other hand, the volcanic ash fallen into the ocean bottom forms a dense seal layer. It isolates the lower organic-rich sediments and upper oxygen-rich water, which also accelerates the preservation of organic matter.

5.2.2 EHST

This section is characterized by intensively developed silty stripes (Fig 4B). Many typical traction structures and geochemical indexes consistently reveal that the ocean floor contour current may have strongly influenced the depositional process of the section EHST. The apparent orientation of graptolite (Fig 4B) indicates the fossils maybe long distance transported. A series of traction structures, for example, minor low-angle cross-bedding (Ma et al., 2016), dwelling burrow and bioturbated (Liu et al., 2017) and silt-mud sharp contact (Fig 5F) are widely developed. The content of feldspar and clay mineral (especially chlorite) significantly enhances (Fig. 3). These sedimentary phenomena indicate that sediments have been transformed just after deposition. Although in the past long time, people believed fine-grain sediments could only deposits in quite water trough suspending transportation (Tyson et al., 1979; Demaison and Moore, 1980). With the deepening of research, more and more scientists consider the laminated mud shale is formed through contour and turbidity current transportation in most conditions (Bohacs 1990; Schieber 1994, 1999; Schieber et al., 2007; Macquaker et al., 2010a, 2010b; Schieber et al., 2011).

The Si_{xs} proxy reveals the primary productivity of this stage reduce to medium level (Fig. 12B). According to the occasional occurrence of thin-layered bentonite (Fig. 4A), the volcanism during this stage has decreased not only in intensity but also in frequency. Due to the lack of nutrients provided by volcanic ash, the primary productivity gradually decreases to a normal level (Wang et al., 2019). The terrigeneous input has a significant improvement (Fig. 12C). During this period, the influences of the ice stage to the global environment is fading out (Brenchley et al., 2003). And the old lands around the Sichuan Basin are continuous uplifting, which is progressed by the Guangxian Movement (Chen et al., 2014). Therefore, a large-scale transgression occurred in the Yangtze area and terrigeneous input enhanced. Geochemical indexes also indicate the environments of bottom marine gradually changes from relatively anoxidation into oxidation (Fig. 11). At the same time, the contour current brings more extrabasinal quartz, feldspar, and clay to the deeper ocean. Because of the sea-level dropping and contour current transformation, the sediment-water contact surface are oxygenated, which accelerates the consumption of organic matter.

5.2.3 LHST

This section is characterized by thick layers of clay-rich mudstone (Fig.3). Wildly distributed turbidite sandstone (Fig. 4C) indicates that the gravity flow usually happens in this section (Plink-Bjorklund et al., 2001; Carvajal and Steel, 2006). In the meantime, current bedding (Fig. 5G) and undulate shaped clays (Fig. 5H) are also indicated further strengthened hydrodynamic condition. The geochemical evidence shows an entirely oxidized benthic environment (Fig 11). With the progressing of the Guangxian Orogeny, the oldlands of the Sichuan Basin margin rapidly uplift, which results in the sharply decreasing of the sea level (Chen et al., 2014; Liu et al., 2017) and copious terrigeneous input. The chemical index of alteration (CIA) is an indicator used to reflect the weathering conditions and paleoclimate in the provenance area (Nesbitt and Young, 1982; Cullers and Podkovyrov, 2002). With the increase of CIA, clay mineral content increase whereas Si_{xs}, and

TOC content decrease (Fig. 13A, B, C). As the CIA proxy shows, the climate suddenly converted from cold and dry to warm and moist, which enhanced the chemical weathering intensity. Combined with the lack of widely covering of lower plants during O-S time, extensively exposed rock also objectively accelerates the terrestrial weathering. As a result, large amounts of terrigenous minerals pours into the ocean, which leads to the significant dilution of organic matter.

5.3 Digenesis lead to further heterogeneity of minerals and organic matter

The minerals and organic matter are furtherly transformed after diagenesis on the base of sedimentation (Schieber, 2010; Loucks et al., 2012), thus intensifying the heterogeneity of the shales in different systems tracts. According to the burial history of the shale in Wufeng-Longmaxi Formation (Guo et al., 2016, Fig. 14A), shales has gone through a relatively complete diagenesis transformation. The Ro of this shale are 2.02%-3.06% (Guo and Zhang, 2014), which is over mature source rock. The organic matter has also undergone a series thermal evolution stage, including kerogen cracking, oil secondary cracking, and other variations (Tissot et al., 1974). Due to the disparity of primary mineral and organic matter composition, the main diagenesis pathway varies in different diagenetic stages of different systems tracts (Fig. 14B).

5.3.1 TST

The formation of organic-rich shale is usually accompanied by a large amount of authentic quartz (Chalmers and Bustin, 2008; Tian et al., 2013; Dong et al., 2017). And section TST also has a high content of quartz, which plays a key role in middle diagenesis of this section (Fig. 14B2). Quartz content correlates well with the organic content (Fig. 13E) and the Si-Zr ratio is similar to the biogenic source trendline (Fig. 13F), which indicate that the source of silica is likely to be derived from organisms (Yan et al., 2015; Zhao et al., 2017; Wang et al., 2018). Firstly, siliceous ooze (opal-A) derived from bioclasts such as radiolarian and sponge spicule would transform into irregular chalcedony grains (opal-CT). Later on, opal-CT grains would recrystallize to microcrystalline quartz aggregates (Fig. 6B; Schieber 2000; Loucks and Ruppel, 2007; Milliken et al., 2012). During this silica dissolution-recrystallization process, the organic matter is gradually released then filled in those complicated cavities formed by biological dissepiments (Schieber 2000), which isolates the chemical corrosion and biolysis, making the organic matters better preserved. As a result, the authigenic quartz fills in the primary pore space of rigid particles. They form a rigid particle-bracing structure (Fig. 6), which significantly resists the following compaction and effectively preserve the remaining pore space.

The early diagenesis is mainly composed of mechanical compaction and chemical cementation, which significantly reduces the space of primary mineral intergranular pores (Loucks et al., 2012; Chalmers and Bustin, 2015). At the same time, large amounts of authigenic pyrite, calcite, dolomite, and silica were formed. First of all, because of the anoxia condition in this section, the organic matter is consumed through sulfate reduction

$$SO_4^{2-}+2CH_2O=H_2S+2HCO^{3-} \quad (1)$$

and produce H_2S, which would be preserved as framboids pyrite (Berner, 1980; Wilkin and Barnes, 1997) as well as calcite cement (Scotchman et al., 1989; McAllister et al., 2015). There are also some fine-grain clay mineral, carbonate, and pyrite are cemented in this process. Large quantities of fine-grain rhombohedral dolomite (Fig 5D) are yield in dolomitic-siliceous mudstone, which are considered to be formed in the interstitial fluid of sediments (Hendry et al., 2000; Bernoulli et al., 2004; Bojanowski, 2014). Recent studies have also shown that this kind of authigenic dolomite is formed in organic-rich deep-water sediments near the sulfate and methane bacteria reduction zones (Hinrichs and Boetius, 2002; Alperin and Hoehler, 2009; Zhao et al., 2017).

Secondary cracking of oil and kerogen (Pommer and Milliken, 2015; Ko et al., 2016) dominate in the middle-late diagenesis stage in section TST (Fig. 14B3). Based on FIB-SEM and nano-CT observation, solid bitumen with abundant pores is the most common form of organic matter (Fig. 6, Fig 9A). With the increase of temperature and pressure, transportable oil and gas produced from kerogen fill in the remaining pore space. They form migrated organic matter and finally evolve into solid bitumen or pyrobitumen. Later, the solid bitumen itself has developed a large number of organic pores (Fig. 6D), which is regarded as the key factor controlling the formation of shale gas (Javial et al., 2007; Lucks et al., 2012).

5.3.2 EHST

Compared with section TST, extrabasinal component such as plagioclase, K-feldspar, chlorite contents highly increase in shales of the section EHST (Fig. 3). While the quartz content in the EHST is not correlated to TOC content (Fig. 13E), and the Si-Zr ratio distributed between the detrital and biogenic source trendlines, which reveals the possible quartz source of those sections are the mixture of terrigenous quartz and biological quartz (Yang et al., 2018). Detrital quartz, feldspar and other rigid minerals do have a certain inhibition on mechanical compaction at the early diagenesis. However, due to the insufficient supply of silica, the content of authigenic quartz decline. As a result, it only forms a particle-bracing structure in partial place (Fig 14B5). Compared with section TST, most part of shales still experiences strong compaction, which causes more primary pose space loss. What worse, framboids pyrite also decrease because of oxidizing environment. The clay mineral content increase and they are compacted into slots of rigid minerals, which greatly diminish residual space for later oil-filing (Fig. 14B6).

5.3.3 LHST

Shales in this section are dominated by a large number of clay minerals, including illite, chlorite and I-S mixed layer (Fig. 2). Ductile clay minerals experienced strong mechanical compaction. Rigid mineral content such as quartz, feldspar, and pyrite are reduced (Fig.3).They even could not directly contact because most of them are wrapped by overwhelmed clay minerals (Fig 7B). In the middle-late stage of diagenesis, large amounts of original clay minerals are corroded and transformed. Smectite has complicated spatial structure and it is chemically unstable. As the rise of temperature and pressure, smectite will gradually transform into illite and other mixed layer clays (Boles and Franks, 1979), the formula is as follows (Van et al., 2008).

$$\begin{gathered}
1.308[(Al_{3.15}Mg_{0.85})(Si_{8.00})O_{20}(OH)_4(Na_{0.85})2H_2O[\text{smectite}] \\
+(0.06Fe_2O_3+0.56K_2O+0.02CaO)] \\
=[(Al_{4.12}Fe_{0.1}Mg_{0.56})(Si_{7.17})O_{20}(OH)_4(K_{1.47}Na_{0.01}Ca_{0.03})][\text{illite}] \\
+3.29SiO_2+0.56Na_2O+0.55MgO+3.23H_2O \quad (2)
\end{gathered}$$

According to the X-ray diffraction data, the content of K-feldspar decreases upward (Fig. 3), and is almost zero in clay-rich lithofacies. This indicates that the vastly consumed K-feldspar during the illite transformation processes may come from K-feldspar, and produces original microcrystalline quartz in the layers of the original clay mineral. Moreover，this reaction leads to dehydration and collapse of the smectite structure, resulting in clay mineral alignment.

5.4 Implications for nanoporous system of shale reservoirs

The nanoporous system is regarded as a significant factor in shale reservoir evaluation (Loucks et al., 2012; Clarkson et al., 2013; Macquaker et al., 2014; Milliken et al., 2015; Zhao et al., 2017;

Zhang et al., 2018). Different depositional and diagenetic process lead to different nanoporous characteristics of shale reservoir in each systems tracts.

5.4.1 TST

Section TST is considered as the highest quality reservoir with high porosity (Fig. 15), which is the major gas-bearing segment in Jiaoshiba area (Guo, 2013). Based on SEM and nano-CT analysis, the rigid particle-bracing structure is the most significant requirement for the formation and preservation of shale nanoporous system. During the depositional process, high marine productivity leads to siliceous organism booming. Later, their siliceous skeleton is well-preserved in anoxic benthic condition, which provides an abundant source of biogenic silica. On the one hand, the biogenic silica comes from their skeletons is a significant part of the particle support system. On the other hand, the large content of the buried organism is the material basis of the hydrocarbon generation. At the same time, the content of extrabasinal minerals is restricted of low terrigeneous input, resulting in a combination primary pore system of fine-grained rigid minerals matrix pores and organism skeleton voids (Fig. 15B1).

In the diagenesis process, a large number of pyrite framboids preferentially produced in the sulfide reduction zone at the anoxic benthic conditions. Many intercrystalline spaces are preserved inside these fine-grained pyrite aggregates. These spaces are very stable and difficult to be filled or reformed by mechanical compaction. With the increase of buried depth, primary pores are rapidly compressed by increasing mechanical compaction. More than 90% of the primary pores would finally disappear with the evolution of diagenesis (Bridge and Demicco, 2008). However, in this section, plenty of biologically derived microcrystalline quartz wildly formed. This authigenic quartz has harbor-shaped edges and complex spatial structure, which could provide additional pore spaces (Schieber 2000). Moreover, the authigenic quartz together with some large particles (such as terrestrial quartz and feldspar) and pyrite framboids forms a rigid particle-bracing structure (Fig. 14B2). It effectively resists mechanical compaction and avoids further encroaching on primary pores. Therefore, a lot of pores are well preserved as the shape of the plump ellipsoid (Fig. 9A2). Also, some clay mineral intraplatelet pores could be retained at the void of particle-bracing structure (Fig. 6C). Interestingly, pore number obtained by Nano-CT analysis is lowest among the three systems tracts whereas total pore volume is highest (Fig. 10; Table. 1). Owing to rigid particle-bracing structure, most of the pores in section TST is not isolated. Conversely, thousands of pores are connected by throat, forming a complete spatial pore-throat system with large internal space. Later, migrated organic matter wildly filled in the particle-bracing structure and then experience a further thermal evolution. A large number of OM pores are produced, which have a significant contribution to total porosity.

Carbonate minerals such as dolomite and calcite produced in early diagenesis stage would occupy some primary pore space. They may play a certain of supporting role. Due to the instability of carbonate mineral, acidic interstitial fluid (like organic acid formed during hydrocarbon generation process) usually corrodes it in every stage of diagenesis, and create the dissolution pores inside the carbonate grain and dissolved margins (Fig. 7D).

5.4.2 EHST

Compared with section TST, the porosity of shales in section EHST has a notable decline (Fig. 15). Because of the influence of contour current, slit sized quartz and feldspar are wildly occurrence

(Fig. 7A). They are stacked and form primary pores at the depositional process (Fig 15B1). Clay mineral contents, especially chlorite are also greatly increased. In this section, marine productivity decrease and redox condition gradually changed to oxic, leaving siliceous organisms such as radiolarians and sponge spicules dissolved during the settling process from the ocean surface (Schieber, 2000). At the same time, the change of the sedimentary environment also makes the organic matter content significantly decrease in this section.

In diagenesis process, pores in pyrite framboids reduce because the burial environment in EHST become more oxic, which produce fewer framboid aggregates. Terrigenous silty particles such as quartz and feldspar from a rigid mineral skeleton, which has a certain inhibitory effect on mechanical compaction (Fig 15B2). Some primary pores could be preserved. However, due to the lack of supporting from enough secondary siliceous minerals, the rigid particle-bracing structure could only produce in the partial area (Fig. A). This incomplete mineral skeleton structure is easy to be destroyed, and primary pores could be rapidly compressed when mechanical compaction enhanced. Thus bulky connected pore-throat system is broken down to separate part (Fig. 9B). The isolated pore number increase but the total pore volume declined (Fig 10B). Meanwhile, more ductile clay minerals also fill in and occupy much primary pore space. Therefore, during middle-late diagenesis, the remaining pore space for OM migrating and occluding is not enough, leaving OM pores decreased. To sum up, less origin organic matter and relative unstable supporting structure make total porosity decline in this section.

5.4.3 LHST

The porosity of section LHST is significantly reduced except for the short-term transgression segment (Fig. 15). In this section, tectonic uplifting together with warmer and moister climate caused terrigenous input significantly increase (Algeo et al., 2016; Wang et al., 2019), leading extrabasinal clay minerals dominated in sediments (Fig. 15C1). Rapid increasing sedimentary rate leads to greatly dilution of organic matter. Accompanied by oxidized water bodies and continuously reduced productivity, siliceous organism skeleton could not well settle down and preserve in sediments. As a result, there is hardly any source of biogenic silica preserved for rigid particle-bracing structure during the depositional process.

In diagenesis process, a large number of plastic clay minerals experienced strong mechanical compaction. They are compacted and formed a denser plastic aggregate wrapped around and Single rigid particles, such as pyrite, feldspar, and quartz (Fig 8B). Thus, rigid particles even could not contact with each other, let alone forming particle-bracing structure. Clay minerals almost completely occupy primary pores, expect in some edges of rigid grains and inner space of pyrite framboids (Fig. 8). In particular, there are more total pore number but less total pore volume obtained of Nano-CT analysis (Fig. 10C). Due to the lack of enough rigid mineral support, pores are strongly compressed into oblate shape. Most of them have fair sized diameter but their volumes are tiny. Moreover, the pore-throat system is almost entirely destroyed (Fig. 9), leaving an isolating nanoporous system. In further diagenesis stage, the S-I transition leads to smectite dehydration and collapse of its structure, which makes the increase of clay mineral alignment and produces microcrystalline quartz (Worden et al., 2005; Christer et al., 2009). Thus, intraplatelet pores within clay aggregates are further shrunk, reduced or even not developed. The microcrystalline quartz is produced inside clay mineral layers, which may play a supporting role for pores (Christer et al., 2009). Because of the reduction of buried organic matter in deposition and the remaining pore space in early diagenesis, migrated organic matter is only preserved as finely blocks around rigid particles or framboid assemblages. As a result, the OM pores are greatly declined.

6. Conclusions

1. Based on the multiscale of the core, thin section, FE-SEM, and nano-CT analysis, shale in different sequence tracts of Wufeng-Longmaxi Formation has a strong heterogeneity in sedimentary structure, lithofacies, mineral assemblages, and organic matter.

2. Global and regional geological events lead to a strong variation in the sedimentary environment, resulting in a large initial mineral composition difference of shales in different sequence tracts. These events also make a substantial change, which causes organic matter accumulation or depletion.

3. Diagenesis further transforms the minerals and organic matter, which aggravates the shale heterogeneity in different sequence tracts. In section TST, biological opal recrystallization produces authigenic quartz filled in primary interparticle pores. It forms a rigid particle-bracing structure, which effectively resisted compaction and controlled OM migrating. In section EHST, less siliceous supply could not produce enough authigenic quartz, which leads to a partial particle-bracing structure. Clay transformation is dominated in section LHST, leading non-existent of the particle-bracing structure.

4. After the differential depositional and diagenetic process, minerals and organic matter in each systems tract differ, which further contributed to the different nanoporous system. Rigid particle-bracing structure leads to a well-preserved bulk pore-throat system in section TST. Partial particle-bracing structure leads to a separated pore-throat system in section EHST. Overwhelmed

clay filled in most primary pores, leaving an isolated and compacted nanoporous system in section LHST.

Acknowledgments

This research was financially funded by the National Natural Science Foundation of China (41690134, 41821002, 41702155, 41690131), National Science & Technology Specific Project (2016ZX05034002-003).

References

Abouelresh, M.O., Slatt, R.M., 2012. Lithofacies and sequence stratigraphy of the Barnett Shale in east-central Fort Worth Basin, TexasGeohorizon. AAPG Bull. 96 (1), 1–22.

Algeo, T.J., Rowe, H., 2012. Paleoceanographic applications of trace-metal concentration data. Chemical Geology, 324-325: 6-18.

Algeo, T.J., Marenco, P.J., Saltzman, M.R., 2016. Co-evolution of oceans, climate, and the biosphere during the 'Ordovician Revolution': A review. Palaeogeography Palaeoclimatology Palaeoecology, 458: 1-11.

Alperin, M.J., Hoehler, T.M., 2009. Anaerobic methane oxidation by archaea/sulfatereducing bacteria aggregates: 1. Thermodynamic and physical constraints. Am. J. Sci. 309, 869-957.

Bernoulli, D., Gasperini, L., Bonatti, E., Stille, P., 2004. Dolomite formation in pelagic limestone and diatomite, romanche fracture Zone, equatorial Atlantic. Sediment. Res. 74, 924-932.

Brenchley, P.J., Carden, G.A., Hints, L., Kaljo, D., Marshall, J.D., Martma, T., Meidla, T., Nõlvak, J., 2003. High-resolution stable isotope stratigraphy of Upper Ordovician sequences: Constraints on the timing of bioevents and environmental changes associated with mass extinction and glaciation. Geological Society of America Bulletin, 115(1): 89-104.

Bustin, R., Link, C., Goodarzi, F., 1989. Optical properties and chemistry of graptolite periderm following laboratory simulated maturation. Org. Geochem. 14, 355-364.

Boles, J.R., Franks, S.G., 1979. Clay diagenesis in Wilcox sandstones of Southwest Texas; implications of smectite diagenesis on sandstone cementation. J. Sediment. Petrol. 49 (1), 55–70.

Bojanowski, M.J., 2014. Authigenic dolomites in the EoceneeOligocene organic carbon-rich shales from the Polish Outer Carpathians: evidence of past gas production and possible gas hydrate formation in the Silesian basin. Mar. Petrol. Geol. 51, 117-135.

Bridge, J.S., Demicco, R.V., 2008. Earth Surface Processes, Landforms and Sediment Deposits. Cambridge University Press, New York, pp. 830.

Carvajal, C. R., Steel, R. J., 2006. Thick turbidite successions from supply-dominated shelves during sea-level highstand. Geology, 34(8), 665.

Chalmers, G.R., Bustin, R.M., 2007. The organic matter distribution and methane capacity of the Lower Cretaceous strata of Northeastern British Columbia, Canada. Int. J. Coal Geol. 70, 223-239.

Chen, S.B., Zhu, Y.M., Wang, G.Y., Liu, H.L., Wei, W., Fang, J. H., 2012. Structure characteristics and accumulation significance of nanopores in longmaxi shale gas reservoir in the southern Sichuan basin. Journal of China Coal Society, 37(3), 438-444(7). (in Chinese with English abstract).

Chen, X., Fan, J.X., Zhang, Y.D., Wang, H.Y., Chen, Q., Wang, W.H., Liang, F., Guo, W., Zhao, Q., Nie, H.K., 2015. Subdivision and delineation of the wufeng and Longmaxi black shales in the subsurface areas of the Yangtze Platform. Journal of Stratigraphy, 39(4): 351-358

Chen. X., Rong, J Y., Li, Y., Boucot, A.J., 2004. Facies patterns and geography of the Yangtze region, South China, through the Ordovician and Silurian transition. Palaeogeography, Palaeoclimatology, Palaeoecology, 204(3-4): 353-372.

Chalmers, G.R., Bustin, R.M., 2008. Lower Cretaceous gas shales in northeastern British Columbia, Part II: evaluation of regional potential gas resources. Bull. Can. Petrol. Geol. 56, 22-61.

Charvet, J., Shu, L,S., Faure, M., Choulet, F., Wang, B., Lu, H. F., Breton, N.L., 2010. Structural development of the Lower Paleozoic belt of South China: Genesis of an intracontinental orogen. Journal of Asian Earth Sciences, 39(4): 309-330.

Clarkson, C.R., Bustin, R.M., 1999. The effect of pore structure and gas pressure upon the transport properties of coal: a laboratory and modeling study 2. Adsorption rate modeling. Fuel 78, 1345–1362.

Cullers, R.L., Podkovyrov, V.N., 2002. The source and origin of terrigenous sedimentary rocks in the Mesoproterozoic Ui group, southeastern Russia. Precambrian Research, 117(3–4): 157-183.

Curtis, J.B., 2002. Fractured shale-gas systems. AAPG Bull. 86(11), 1921–1938.

Demaison, G.J., Moore, G.T., 1980. Anoxic environments and oil source bed genesis. Organic Geochemistry, 2(1): 9-31.

Dong, T., Harris, N.B., Ayranci, K., 2017. Relative sea-level cycles and organic matter accumulation in shales of the Middle and Upper Devonian Horn River Group, northeastern British Columbia, Canada: Insights into sediment flux, redox conditions, and bioproductivity. Geological Society of America Bulletin, 81:220-236.

Duggen, S., 2007. Drastic shift in lava geochemistry in the volcanic-front to rear-arc region of the

Southern Kamchatkan subduction zone: Evidence for the transition from slab surface dehydration to sediment melting. Geochimica et Cosmochimica Acta, 71(2): 452-480.

Fan, J.X., Melchin, M.J.,Chen, X.,Wang, Y.,Zhang, Y. D.,Chen, Q.,Chi, Z. L.,Chen, F.,2011. Biostratigraphy and geography of the Ordovician-Silurian Longmaxi black shales in South China. Science China Earth Sciences, 54(12): 1854-1863.

Fishman, N.S., Egenhoff, S.O., Boehlke, A.R. Lowers, H.A., 2015. Petrology and diagenetic history of the upper shale member of the late Devonian-early Mississippian Bakken Formation, Williston Basin, North Dakota. Special Paper of the Geological Society of America, 515(4): 125-151.

Guo, T.L., 2013. Evaluation of highly thermally mature shale-gas reservoirs in complex structural parts of the Sichuan Basin. Journal of Earth Science, 24(6): 863-873.

Guo, T.L., Zhang, H.R., 2014. Formation and enrichment mode of Jiaoshiba shale gas field, Sichuan Basin. Petroleum Exploration & Development, 41(1): 31-40.

Guo, X., Hu, D., Li, Y., Wei, X., Wang, Q., Zhang, H., 2016. Technologies in discovery and exploration of Fuling Shale Gas Field, China. Nat. Resour. 7, 271-286.

Hammes, U., Frébourg, G., 2012. Haynesville and Bossier mudrocks: a facies and sequence stratigraphic investigation, East Texas and Louisiana, USA. Mar. Pet. Geol. 31 (1), 8–26.

Hao, F., Zou, H.Y., Lu, Y.C., 2013. Mechanisms of shale gas storage: implications for shale gas exploration in China. AAPG Bull. 97 (8), 1325–1346.

Haq, B.U., Schutter, S.R., 2008. A chronology of Paleozoic sea-level changes. Science, 322(5898): 64-68.

Hendry, J.P., Wilkinson, M., Fallick, A.E., Trewin, N.H., 2000. Disseminated ‘jigsaw piece’dolomite in Upper Jurassic shelf sandstones, Central North Sea: an example of cement growth during bioturbation? Sedimentology 47, 631-644.

Hinrichs, K.U., Boetius, A., 2002. The anaerobic oxidation of methane: new insights in microbial ecology and biogeochemistry. In: Ocean Margin Systems. Springer, pp. 457-477.

Jarvie, D.M., Hill, R.J., Ruble, T.E., Pollastro, R.M., 2007. Unconventional shale-gas systems: the Mississippian Barnett Shale of north-central Texas as one model for thermogenic shale-gas assessment. AAPG Bull. 91(4), 475–499.

Jiang, Z. X., Tang, X. L., Cheng, L.J., Li, Z., Zhang, Y.Y., Bai, Y. Q., Yuan, Y., Hao, Jin., 2015. Characterization and origin of the silurian wufeng-longmaxi formation shale multiscale heterogeneity in Southeastern Sichuan Basin, China. Interpretation, 3(2), SJ61-SJ74.

Ko, L., Loucks, R., Zhang, T. W., Ruppel, S., Shao, D., 2016. Pore and pore network evolution of upper cretaceous boquillas (eagle ford-equivalent) mudrocks: results from gold tube pyrolysis experiments. AAPG Bulletin, 100(1-11), 1693-1722.

Langmann, B., Zakšek, K., Hort, M., 2010. Atmospheric distribution and removal of volcanic ash after the eruption of Kasatochi volcano: A regional model study, 4447-4458 pp.

Li, P., and Z. J. Jin, 2003. The present research status and progress of petroleum exploration in the Jiyang Depression: Petroleum Exploration and Development, 30, 1–4.

Li, Z.X., Wartho, J.A., Clark, C., Li, W.X., Zhang, C.L., Bao, C., 2010. Magmatic and metamorphic events during the early Paleozoic Wuyi-Yunkai orogeny, southeastern South China: New age constraints and pressure-temperature conditions. Geological Society of America Bulletin, 122(5-6): 772-793.

Liu, S.G., Ma, W.X., Jansa, L., Huang, W., Zeng, X., Zhang, C., 2013. Characteristics of the shale gas reservoir rocks in the lower silurian longmaxi formation, east sichuan basin, china. Energy, Exploration & Exploitation, 31(2), 187-220 (in Chinese with English abstract).

Liu, Z.H., Algeo, T.J., Guo, X.S., Fan, J.X., Du, X.B., Lu, Y.C., 2017. Paleo-environmental cyclicity in the Early Silurian Yangtze Sea (South China): Tectonic or glacio-eustatic control? Palaeogeography, Palaeoclimatology, Palaeoecology, 466: 59-76.

Loucks, R.G., Reed, R.M., Ruppel, S.C., Hammes, U., 2012. Spectrum of pore types and networks in mudrocks and a descriptive classification for matrix-related mudrock pores. Am. Assoc. Petrol. Geol. Bull. 96, 1071-1098.

Loucks, R.G., Ruppel, S.C., 2007. Mississippian Barnett Shale: lithofacies and depositional setting of a deep-water shale-gas succession in the Fort Worth Basin, Texas. Am. Assoc. Petrol. Geol. Bull. 91, 579-601.

Lu, Y.B., Ma, Y.Q., Wang, Y.X., Lu, Y.C., 2017. The sedimentary response to the major geological events and lithofacies characteristics of Wufeng Formation-Longmaxi Formation in the upper Yangtze area.

Ross, D.J.K., Bustin, R.M., 2009. Investigating the use of sedimentary geochemical proxies for paleoenvironment interpretation of thermally mature organic-rich strata: Examples from the Devonian–Mississippian shales, Western Canadian Sedimentary Basin. Chemical Geology, 260(1-2): 1-19.

Rong, J.Y., 2006. Re-evaluation of survivors, Lazarus taxa, and refugia from mass extinction. Earth Science Frontiers, 111(B8): 1-32.

Ma, Y.Q., Fan, M.J., Lu, Y.C., Guo, X.S., Hu, H.Y., Chen, L., Wang, C., Liu, X. C., 2016. Geochemistry and sedimentology of the Lower Silurian Longmaxi mudstone in southwestern China: Implications for depositional controls on organic matter accumulation. Marine and Petroleum Geology, 75: 291-309.

Ma, Y., Pan, Z., Zhong, N., Connell, L. D., Down, D. I., Lin, W., et al. Experimental study of anisotropic gas permeability and its relationship with fracture structure of Longmaxi shales, Sichuan Basin, China. Fuel 2016; 180: 106-115.

Macquaker, J. H. S., S. J. Bentley, K. M. Bohacs, 2010a. Wave-enhanced sediment-gravity flows and mud dispersal across continental shelves: Reappraising sediment transport processes operating in ancient mudstone successions: Geology, 38:947–950

Macquaker, J. H. S., M. A. Keller, and S. J. Davies, 2010b. Algal blooms and “marine snow”: Mechanisms that enhance organic carbon preservation in ancient fine-grained sediments: Journal of Sedimentary Research, 80:934–942,

Macquaker, J.H.S., Taylor, K.G., Keller, M., Polya, D., 2014. Compositional controls on early diagenetic pathways in fine-grained sedimentary rocks: implications for predicting unconventional reservoir attributes of mudstones. Am. Assoc. Petrol. Geol. Bull. 98, 587-603.

McAllister, R.T., Taylor, K., Garcia-Fresca, B., Hollis, C., 2015. Diagenetic evolution of the Eagle Ford formation. In: SW Texas: Impacts upon Reservoir Quality and Rock Properties. Unconventional Resources Technology Conference, 20-22 July. URTec 2153115, San Antonio, Texas, USA.

Middleton G V., 1976. Hydraulic Interpretation of Sand Size Distributions. The Journal of Geology, 84(4):405-426.

Milliken, K.L., Esch, W.L., Reed, R.M., Zhang, T., 2012. Grain assemblages and strong diagenetic overprinting in siliceous mudrocks, Barnett Shale (Mississippian), Fort Worth Basin, Texas. Am. Assoc. Petrol. Geol. Bull. 96, 1553-1578.

Milliken, K.L., Wang, X., Shen, Y., Liang, Q., Zhang, T., Loucks, B., Rowe, H., 2015. Grain assemblages in organic-rich mudstones dominated by extrabasinal Sediment Sources, Yanchang Formation (Triassic), Ordos Basin, China. In: AAPG International Conference and Exhibition, 13-15 September, 2015, Melbourne, Australia.

Nesbitt Amp, H.W., Young, G.M., 1982. Early proterozoic climates and plate motions inferred from major element chemistry of lutites. Nature, 299(5885): 715-717.

Peltonen, C., Marcussen, Ø., Bjørlykke, K., Jahren, J., 2009. Clay mineral diagenesis and quartz cementation in mudstones: the effects of smectite to illite reaction on rock properties. Mar. Petrol. Geol. 26, 887-898.

Plink-Bjorklund, P., Mellere, D., Steel, R. J., 2001. Turbidite variability and architecture of sand-prone, deep-water slopes: eocene clinoforms in the central basin, spitsbergen. Journal of Sedimentary Research, 71(6), 895-912.

Pommer, M., Milliken, K., 2015. Pore types and pore-size distributions across thermal maturity, Eagle Ford Formation, southern Texas. AAPG Bulletin, 99(9), 1713-1744

Schieber, J., 1994. Evidence for high-energy events and shallow-water deposition in the Chattanooga Shale, Devonian, central Tennessee, USA. Sedimentary Geology, 93(3-4), 193-

208.

Schieber, J., 1999. Distribution and deposition of mudstone facies in the Upper Devonian Sonyea Group of New York. Journal of Sedimentary Research, 69(4):909-925.

Schieber, J., Krinsley, D., Riciputi, L., 2000. Diagenetic origin quartz silt in mudstones and implications for silica cycling. Nature, 406(6799), 981-985.

Schieber, J., Southard, J., Thaisen, K., 2007. Accretion of Mudstone Beds from Migrating Floccule Ripples. Science, 318(5857):1760-1763.

Schieber, J., 2010. Common themes in the formation and preservation of intrinsic porosity in shales and mudstones-Illustrated with examples across the Phanerozoic. In: SPE Unconventional Gas Conference. Society of Petroleum Engineers.

Schieber, J., 2011. Reverse engineering mother nature —Shale sedimentology from an experimental perspective. Sedimentary Geology, 238(1-2):1-22.

Scotchman, I., Johnes, L., Miller, R., 1989. Clay diagenesis and oil migration in brent group sandstones of NW Hutton Field, UK North Sea. Clay Miner. 24, 339-374.

Slatt, R.M., Rodriguez, N.D., 2012. Comparative sequence stratigraphy and organic geochemistry of gas shales: commonality or coincidence? J. Nat. Gas. Sci. Eng. 8, 68–84.

Shebl, M. A., Yalavarthi, R., Nyaaba, C., 2013. Role of detailed reservvoir characterization and lateral placement on well performance in the Marcellus Shale Gas Reservoir. SPE 16718.

Sun, L., Wang, X., Jin, X., Li, J., Wu, S. Three dimensional characterization and quantitative connectivity analysis of micro/nano pore space. Petroleum Exploration and Development 2016; 43(3): 537-546.

Su, W. B., Huff, W.D., Ettensohn, F. R., Liu, X. M., Zhang, J.E., Li, Z.M., 2009. K-bentonite, black-shale and flysch successions at the Ordovician–Silurian transition, South China: Possible sedimentary responses to the accretion of Cathaysia to the Yangtze Block and its implications for the evolution of Gondwana. Gondwana Research, 15(1): 111-130.

Tian, H., Pan, L., Xiao, X., Wilkins, R.W., Meng, Z., Huang, B., 2013. A preliminary study on the pore characterization of Lower Silurian black shales in the Chuandong Thrust Fold Belt, southwestern China using low pressure N2 adsorption and FE-SEM methods. Mar. Petrol. Geol. 48, 8-19.

Tissot, B., Durand, B., Espitalie, J., Combaz, A., 1974. Influence of nature and diagenesis of organic matter in formation of petroleum. Am. Assoc. Petrol. Geol. Bull. 58, 499-506.

Tribovillard, N., Algeo, T.J., Lyons, T., Riboulleau, A., 2006. Trace metals as paleoredox and paleoproductivity proxies: An update. Chemical Geology, 232(1-2): 12-32.

Turgeon, S., Brumsack, H.J., 2006. Anoxic vs dysoxic events reflected in sediment geochemistry during the Cenomanian–Turonian Boundary Event (Cretaceous) in the Umbria–Marche Basin of central Italy. Chemical Geology, 234(3): 321-339.

Tyson, R.V., 2001. Sedimentation rate, dilution, preservation and total organic carbon: some results of a modelling study. Organic Geochemistry, 32(2): 333-339.

Van, D.B., S.H.J.M, Van, B.M.J., Nijman, W., Vroon, P.Z., 2007. Dual role of seawater and hydrothermal fluids in Early Archean chert formation: evidence from silicon isotopes. Geology 35, 939–942.

Walleed, F., 2011. Innovative reservoir modeling and simulation of unconventional shale gas reservoirs powered by microseismic data. SPE 141788.

Wang, Y.X., Xu, S., Hao, F., Lu, Y.B., Shu, Z.G., Yan, D.T., Lu, Y.C., 2019. Geochemical and petrographic characteristics of Wufeng-Longmaxi shales, Jiaoshiba area, southwest China: Implications for organic matter differential accumulation. 102:138-154.

Wilkin, R., Barnes, H., 1997. Formation processes of framboidal pyrite. Geochim. Cosmochim. Acta 61, 323-339.

Worden, R.H., Charpentier, D., Fisher, Q.J., Aplin, A.C., 2005. Fabric development and the smectite to illite transition in Upper Cretaceous mudstones from the North Sea: an image analysis approach. In: Understanding the Micro to Macro Behavior of Rock–fluid Systems. Geological Society of London, Special Publications, pp. 103–114. London, United Kingdom.

Yan, D.T., Wang, H., Fu, Q.L., Chen, Z.H., He, J., Gao, Z., 2015. Geochemical characteristics in the Longmaxi formation (early silurian) of south China: implications for organic matter accumulation. Mar. Petrol. Geol. 65, 290–301.

Yang, X.R., Yan, D.T., Wei, X.S., Zhang, L.W., Zhang, Bao., Xu, H.W., Gong, Yin., He, Jie., 2015. Different formation mechanism of quartz in siliceous and argillaceous shales: A case study of Longmaxi Formation in South China. Mar. Petrol. Geol. 94, 80–94.

Zhang, L.C., Li, B., Jiang, S., Xiao, D.S., Lu, S.F., Zhang, Y.Y., Gong, C., Chen, L., 2018. Heterogeneity characterization of the lower Silurian Longmaxi marine shale in the Pengshui area, South China. 195:250-266.

Zou, C.N., Dong, D.Z., Wang H.Y., Wang, Y.M., Wang, S.F., Li, X.J., Huang, J.L., Guan, Q.Z., Zhang, C.C Liu, D.X., Liu, H.L., Bai, W.H., Liang, P.P., Liang, F., Lin, W., Zhao, Q., Yang, Z., Sun, S.S., Qiu, Z., 2016. Shale gas in China: Characteristics, challenges and prospects (II)., 43(2): 182-196.

Figure captions

Figure 1. (A) Thickness distribution of organic-rich shales of the Wufeng-Longmaxi Formation in the upper Yangtze area. (B) Stratigraphic column of the Wufeng and Longmaxi formation.

Figure 2. Stratigraphic framework construction of the Wufeng and Longmaxi formation in Jiaoshiba

Area of well A through a comprehensive interpretation over well logging, lithology and graptolite zonation. GR = Natural gammy ray logging; AC = Acoustic logging; CNL=Neutron logging; MFS = maximum flooding surface; SFS = sub flooding surface.

Figure 3. Mineral and organic matter contents variation within the stratigraphic framework.

Figure 4. Heterogeneity characteristics in core scale observation. (A) Core photograph shows distinctive bentonite layers (arrows) in TST. Guangyinqiao bedding is marked by a dotted line, which is considered to be the lithology key bed of Ordovician-Silurian Boundary. (B) Core photograph shows abundant laminas and oriented graptolites fossils. (C) Core photograph shows turbidite sandstone interbedded in shale and disorganizing stacked graptolites fossils.

Figure 5. Heterogeneity characteristics in thin section scale observation. (A) Fine-grained and evenly distributed mineral and organic-matter particles (Siliceous mudstone). (B) Organic matter and calcite occupied cavities (arrows), which come from radiolarians. (C) Organic matter filled sponge spicules (arrows). (D) Fine sized dolomite grains (arrows). (E) Silt stripes. (F) Abruptly non-invasion top contact (dotted line) and lenticular intraclast (arrows). (G) current bedding (H) abundant distributed clay lenticulars (arrows). Picture C and D are cited from Ma et al., 2016.

Figure 6. Heterogeneity characteristics of TST shales in FIB-SEM scale observation. (A) Rigid particle-bracing structure in TST (overall view). (B) Rigid particle-bracing structure in TST (partial view). (C) Microfractures preserved in clay minerals. (D) Migrated organic matter and organic matter pores.

Figure 7. Heterogeneity characteristics of EHST shales in FIB-SEM scale observation. (A) Partial particle-bracing structure (overall view). (B) Particle-bracing-structure in TST (partial view). (C) Primary pore space preserved around the pyrite. (D) Carbonate cementation: authigenic dolomite overgrown by rhomb Fe-dolomite and dissolution pores in calcite.

Figure 8. Heterogeneity characteristics of LHST shales in FIB-SEM scale observation. (A) No particle-bracing structure (overall view). (B) No particle-bracing structure (partial view). Quartz, Feldspar, and calcite are completely wrapped by clay mineral. (C) Pore space preserved around the pyrite in LHST. (D) Pore space preserved inside framboid assemblage.

Figure 9. Reconstructed 3D Organic matter (blue) and pore (red) and pore connectivity (stick model) distribution in section TST, EHST, and LHST. The pores are represented by blue dotes. The big throat is a bright white line, the middle throat is an orange line, and the small throat is an orange-red line.

Figure 10. Pore number and pore volume distribution of shales obtained by Nano-CT in each systems tract. (A) Pore number and pore volume distribution in section TST. (B) Pore number and pore volume distribution in section EHST. (C) Pore number and pore volume distribution

in section LHST.

Figure 11. Geochemical proxies for marine redox condition variation from TST to LHST. (A) Corg-S-Fe relationships, where Corg refer to total organic carbon (TOC) content. (B) Enrichment factors (EFs) of Mo versus U. The lines exhibit Mo/U ratios equal to seawater (SW). The patterns of U-EF and Mo-EF are compared to the model of Algeo and Tribovillard (2009). (C) Crossplot of Corg/P and Th/U ratios used as paleoredox proxies for the samples from Wufeng-Longmaxi Formation in Jiaoshiba area.

Figure 12. Climate change form Wufeng Formation to Longmaxi Formation triggers minerals and organic matter in differential input at different systems tracts.

Figure 13. The relationships of TOC content to Th/U, Sixs and Al2O3 in different systems tracts of Wufeng-Longmaxi formation in Jiaoshiba area.

Figure 14. (A) Burial history of Wufeng-Longmaxi shale (modified from Guo et al., 2016). (B) A conceptual model of the depositional and diagenetic process of shales in different systems tracts.

Figure 15. Porosity variation and its relationship of TOC, clay mineral and quartz content of samples in Well A.

Table captions

Table 1. Pore characteristics of samples in Wufeng-Longmaxi Formation obtained by Nano-CT analysis.

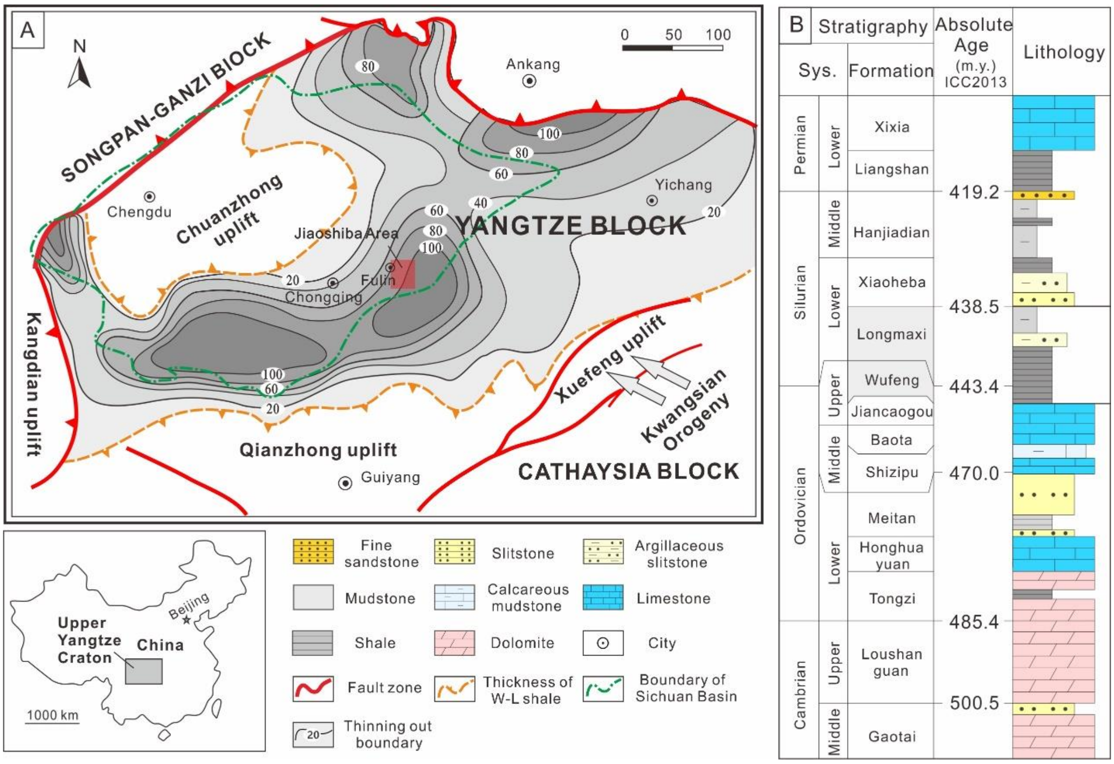

Figure 1. (A) Thickness distribution of organic-rich shales of the Wufeng-Longmaxi Formation in the upper Yangtze area. (B) Stratigraphic column of the Wufeng and Longmaxi formation.

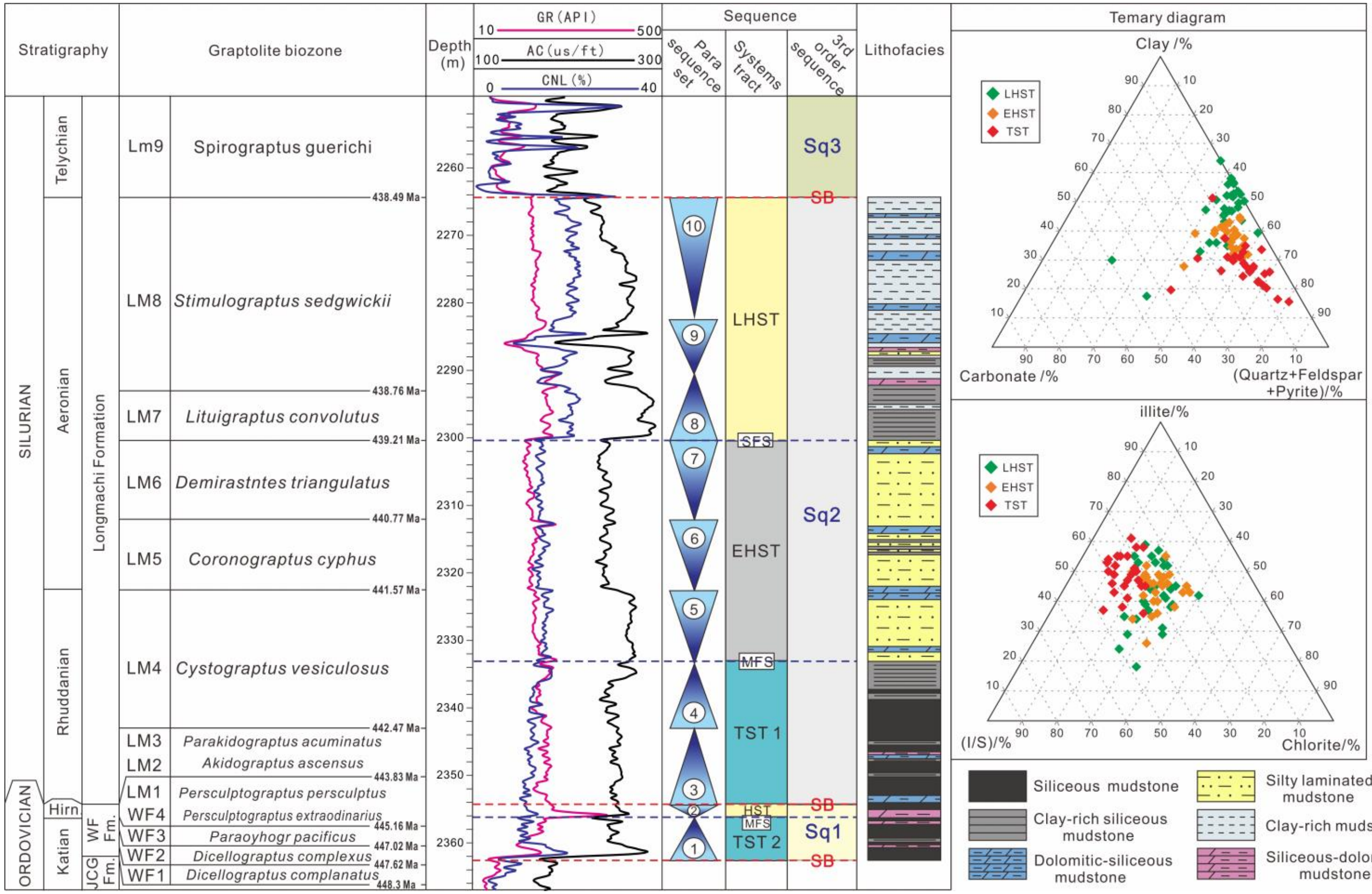

Figure 2. Stratigraphic framework construction of the Wufeng and Longmaxi formation in Jiaoshiba Area of well A through a comprehensive interpretation over well logging, lithology and graptolite zonation. GR = Natural gammy ray logging; AC = Acoustic logging; CNL=Neutron logging; MFS = maximum flooding surface; SFS = sub flooding surface.

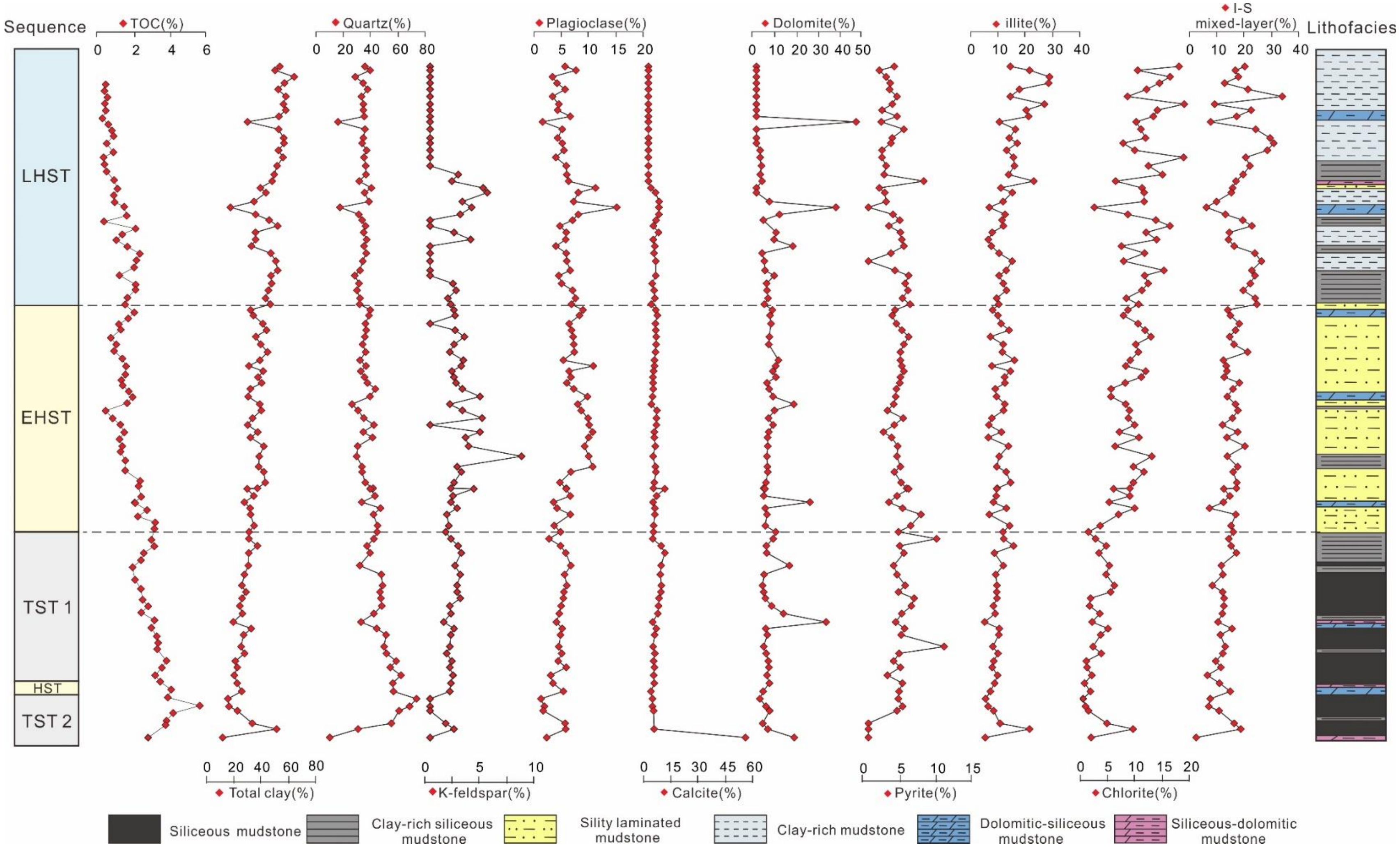

Figure 3. Mineral and organic matter contents variation within the stratigraphic framework.

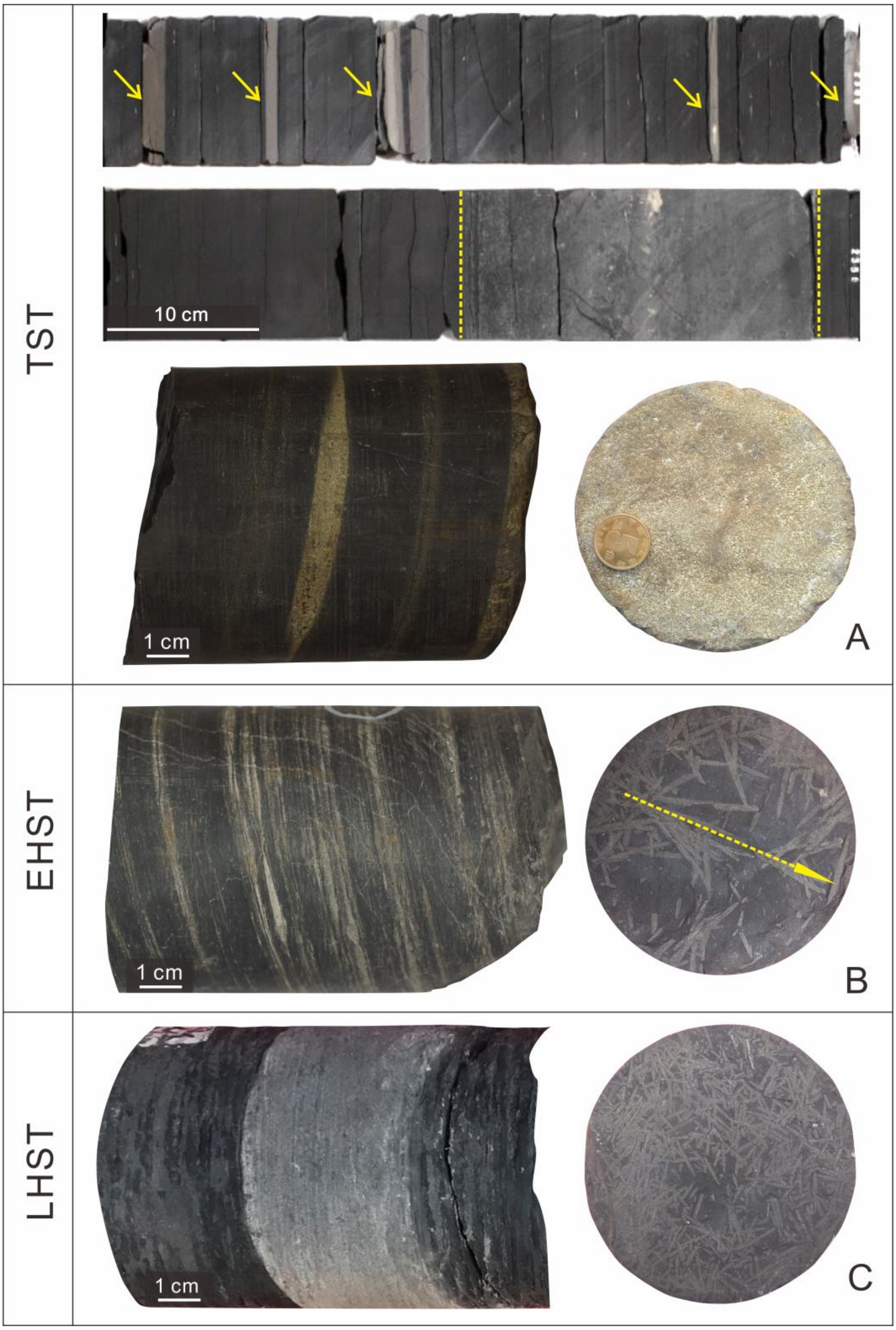

Figure 4. Heterogeneity characteristics in core scale observation. (A) Core photograph shows distinctive bentonite layers (arrows) in TST. Guangyinqiao bedding is marked by a dotted line, which is considered to be the lithology key bed of Ordovician-Silurian Boundary. (B) Core photograph shows abundant laminas and oriented graptolites fossils. (C) Core photograph shows turbidite sandstone interbedded in shale and disorganizing stacked graptolites fossils.

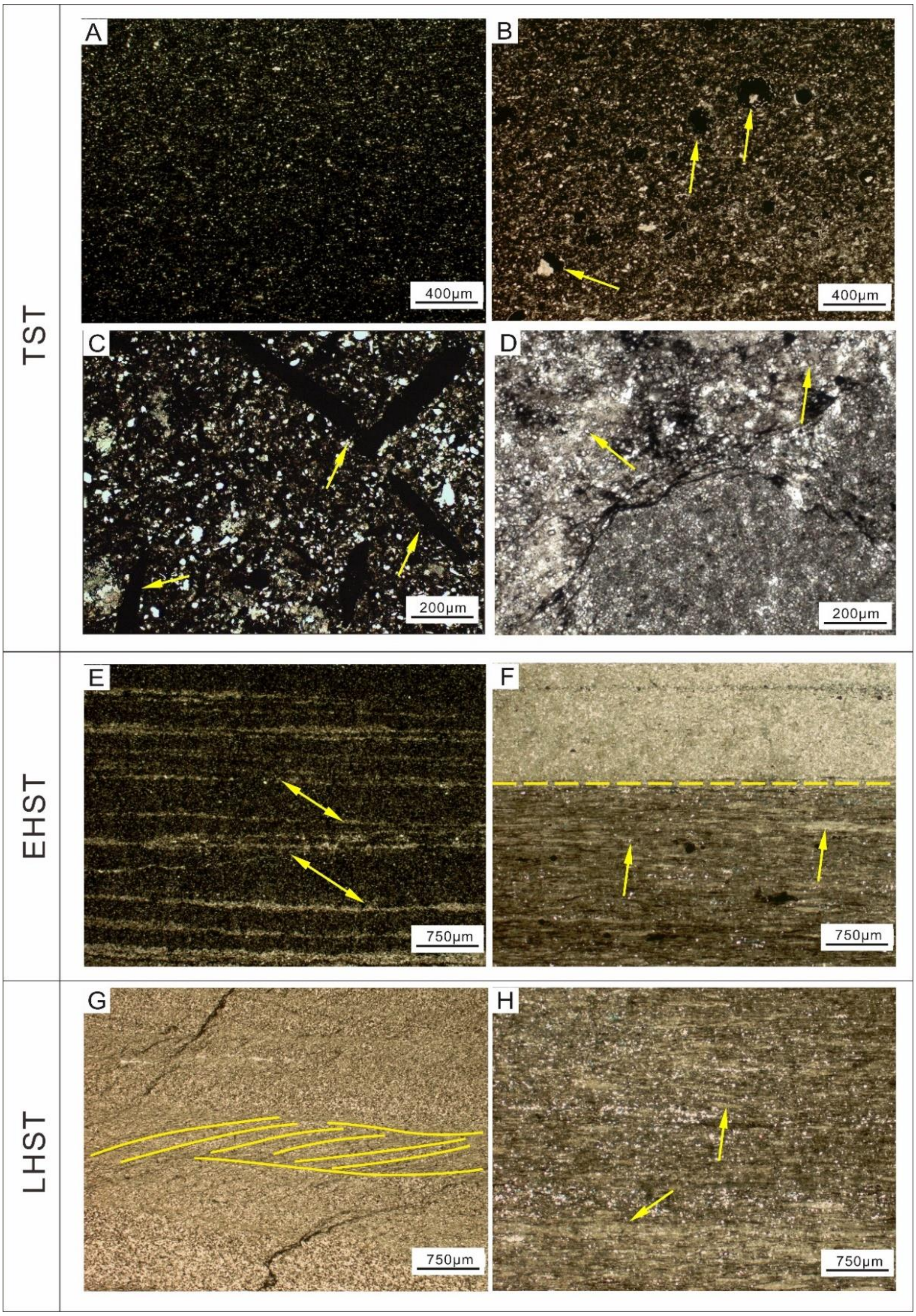

Figure 5. Heterogeneity characteristics in thin section scale observation. (A) Fine-grained and evenly distributed mineral and organic-matter particles (Siliceous mudstone). (B) Organic matter and calcite occupied cavities (arrows), which come from radiolarians. (C) Organic matter filled sponge spicules (arrows). (D) Fine sized dolomite grains (arrows). (E) Silt stripes. (F) Abruptly non-invasion top contact (dotted line) and lenticular intraclast (arrows). (G) current bedding (H) abundant distributed clay lenticulars (arrows). Picture C and D are cited from Ma et al., 2016.

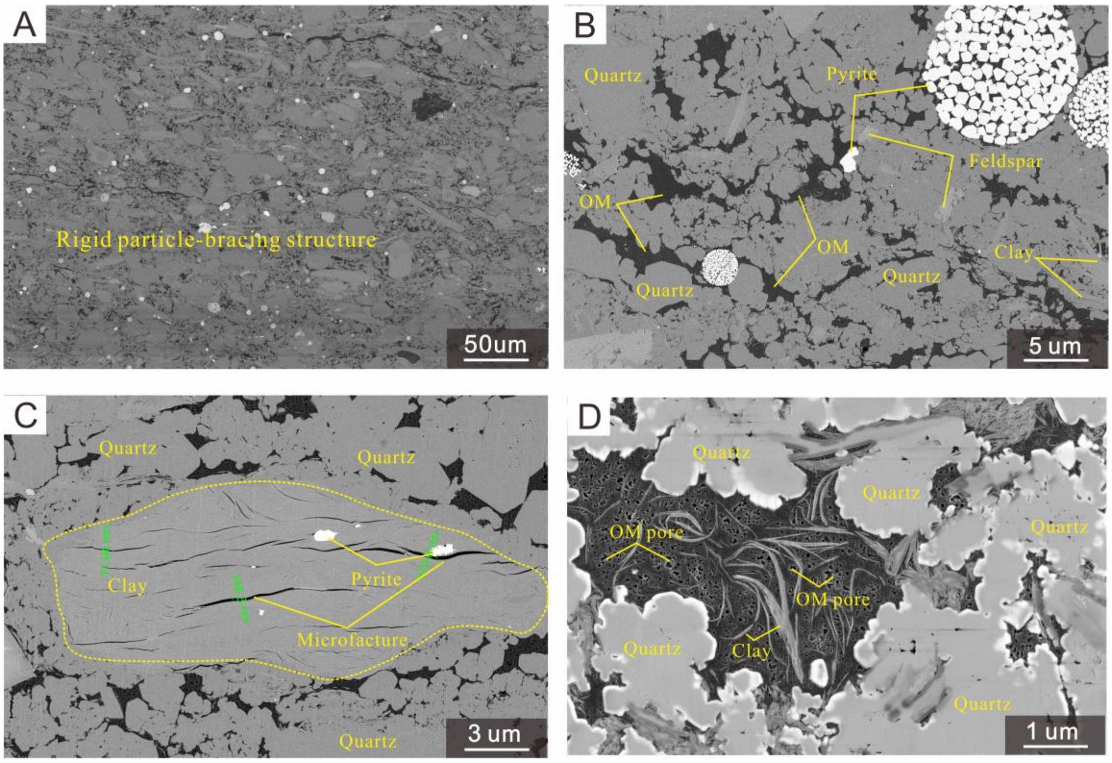

Figure 6. Heterogeneity characteristics of TST shales in FIB-SEM scale observation. (A) Rigid particle-bracing structure in TST (overall view). (B) Rigid particle-bracing structure in TST (partial view). (C) Microfractures preserved in clay minerals. (D) Migrated organic matter and organic matter pores.

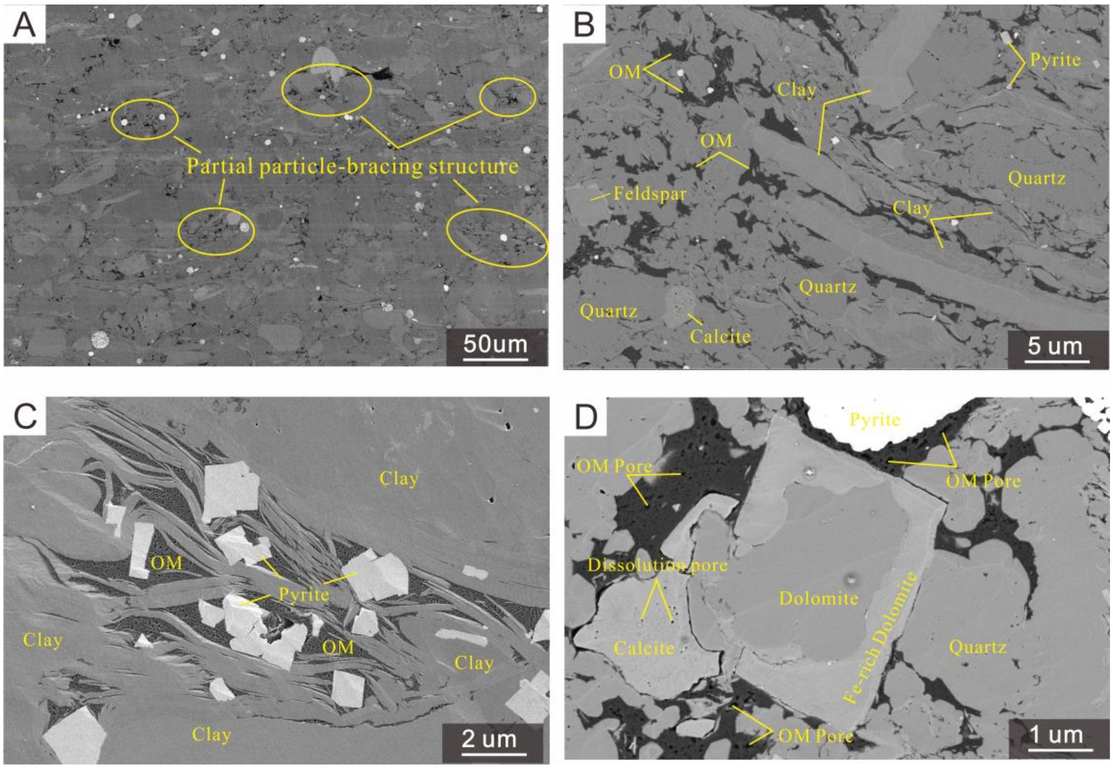

Figure 7. Heterogeneity characteristics of EHST shales in FIB-SEM scale observation. (A) Partial particle-bracing structure (overall view). (B) Particle-bracing-structure in TST (partial view). (C) Primary pore space preserved around the pyrite. (D) Carbonate cementation: authigenic dolomite overgrown by rhomb Fe-dolomite and dissolution pores in calcite.

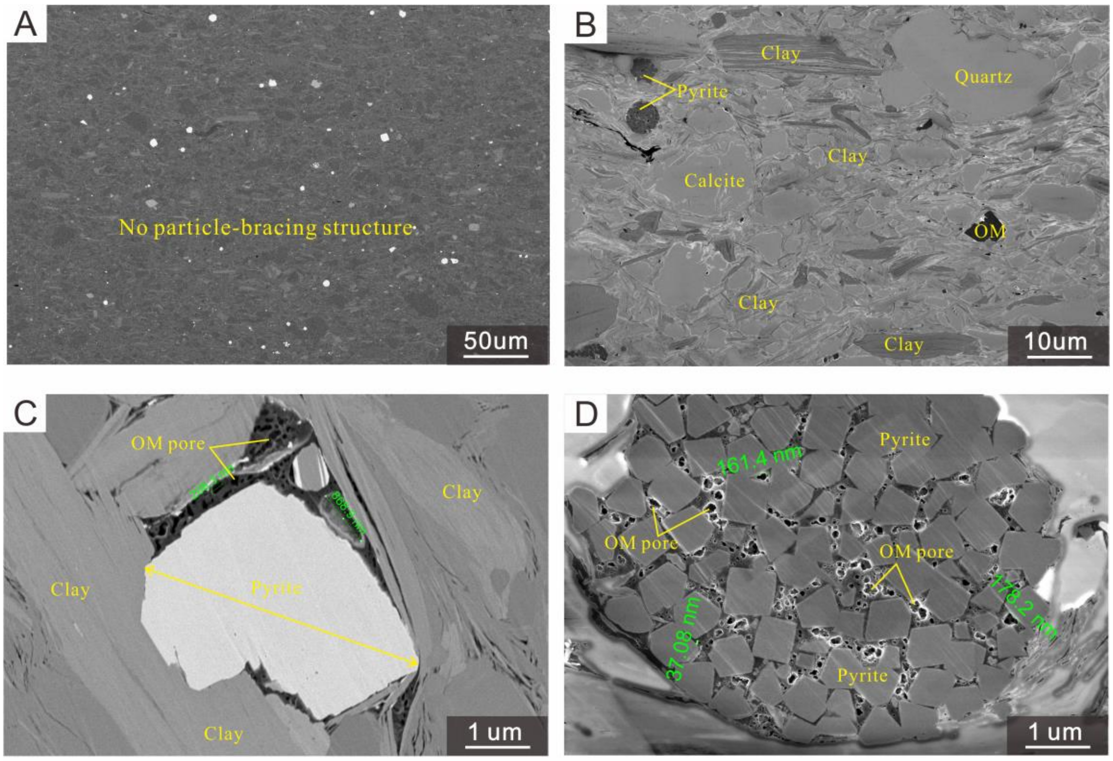

Figure 8. Heterogeneity characteristics of LHST shales in FIB-SEM scale observation. (A) No particle-bracing structure (overall view). (B) No particle-bracing structure (partial view). Quartz, Feldspar, and calcite are completely wrapped by clay mineral. (C) Pore space preserved around the pyrite in LHST. (D) Pore space preserved inside framboid assemblage.

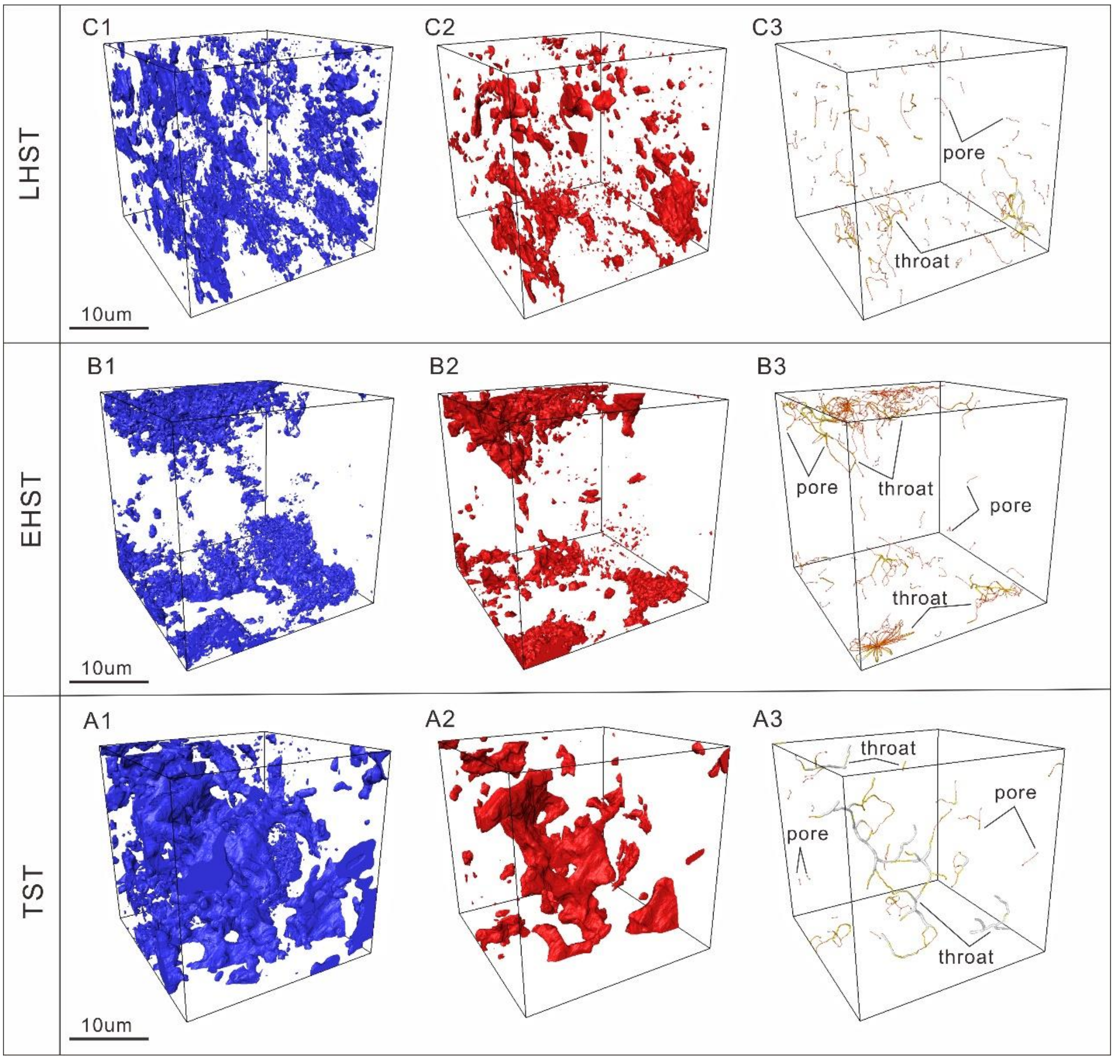

Figure 9. Reconstructed 3D Organic matter (blue) and pore (red) and pore connectivity (stick model) distribution in section TST, EHST, and LHST. The pores are represented by blue dotes. The big throat is a bright white line, the middle throat is an orange line, and the small throat is an orange-red line.

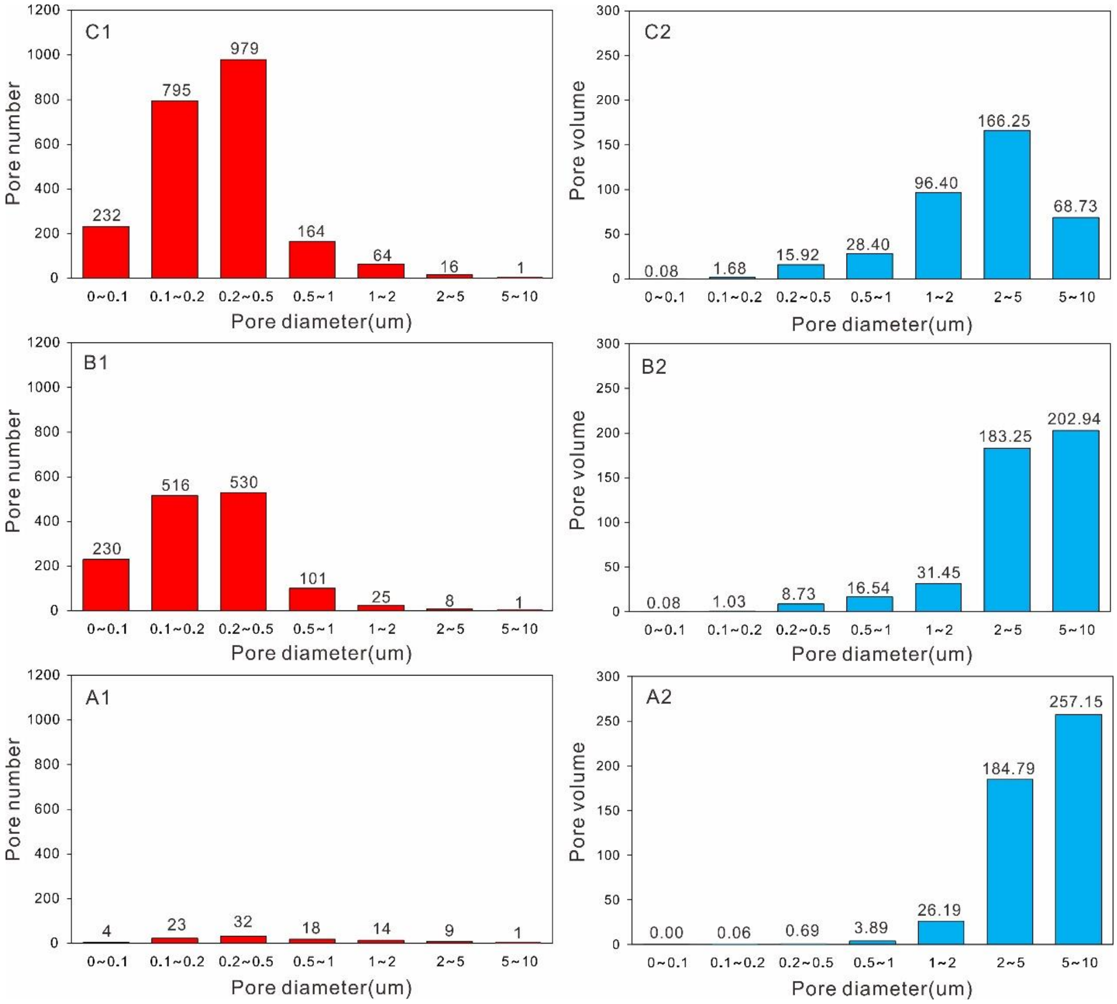

Figure 10. Pore number and pore volume distribution of shales obtained by Nano-CT in each systems tract. (A) Pore number and pore volume distribution in section TST. (B) Pore number and pore volume distribution in section EHST. (C) Pore number and pore volume distribution in section LHST.

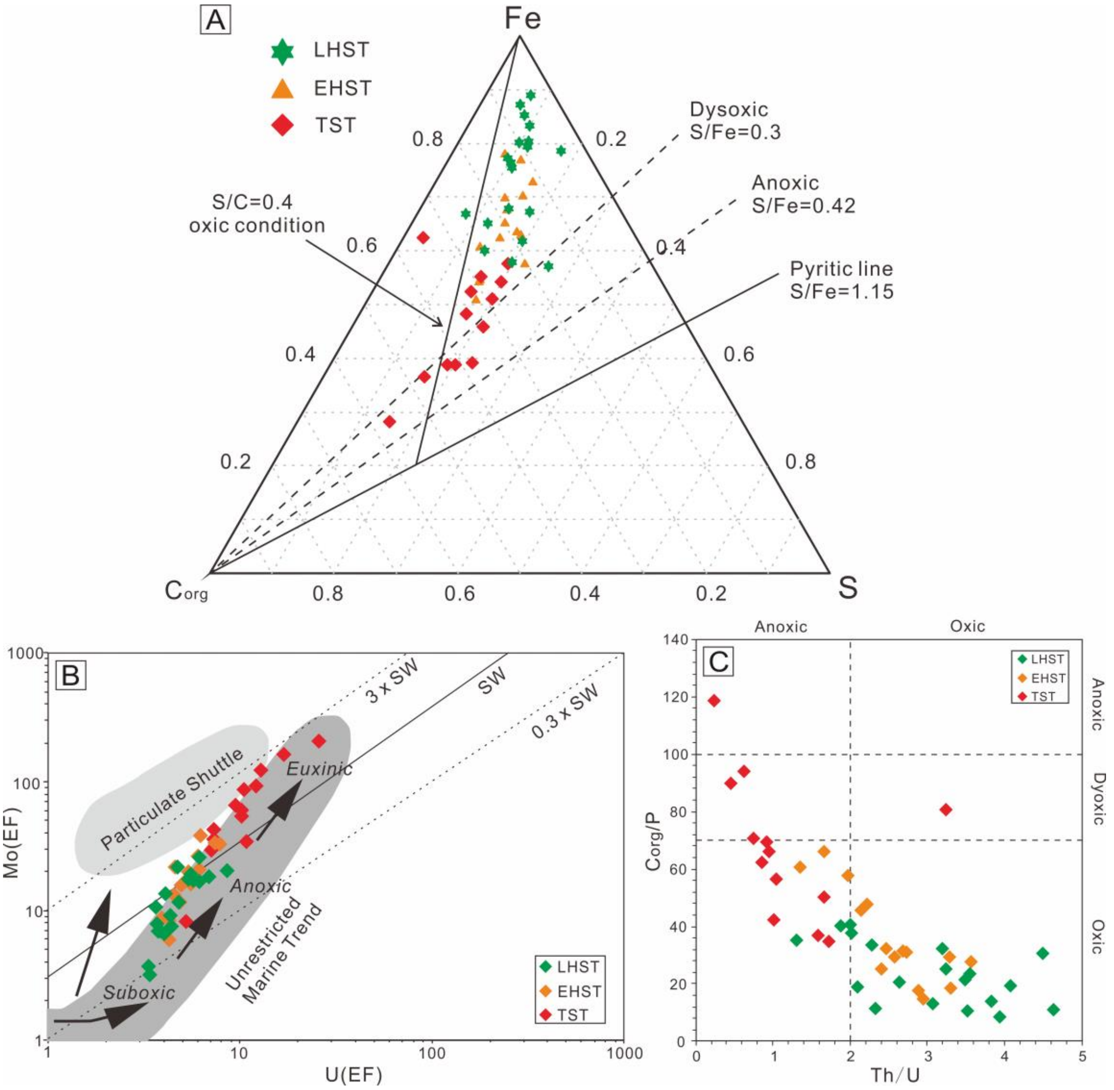

Figure 11. Geochemical proxies for marine redox condition variation from TST to LHST. (A) C_{org}-S-Fe relationships, where C_{org} refer to total organic carbon (TOC) content. (B) Enrichment factors (EFs) of Mo versus U. The lines exhibit Mo/U ratios equal to seawater (SW). The patterns of U-EF and Mo-EF are compared to the model of Algeo and Tribovillard (2009). (C) Crossplot of C_{org}/P and Th/U ratios used as paleoredox proxies for the samples from Wufeng-Longmaxi Formation in Jiaoshiba area.

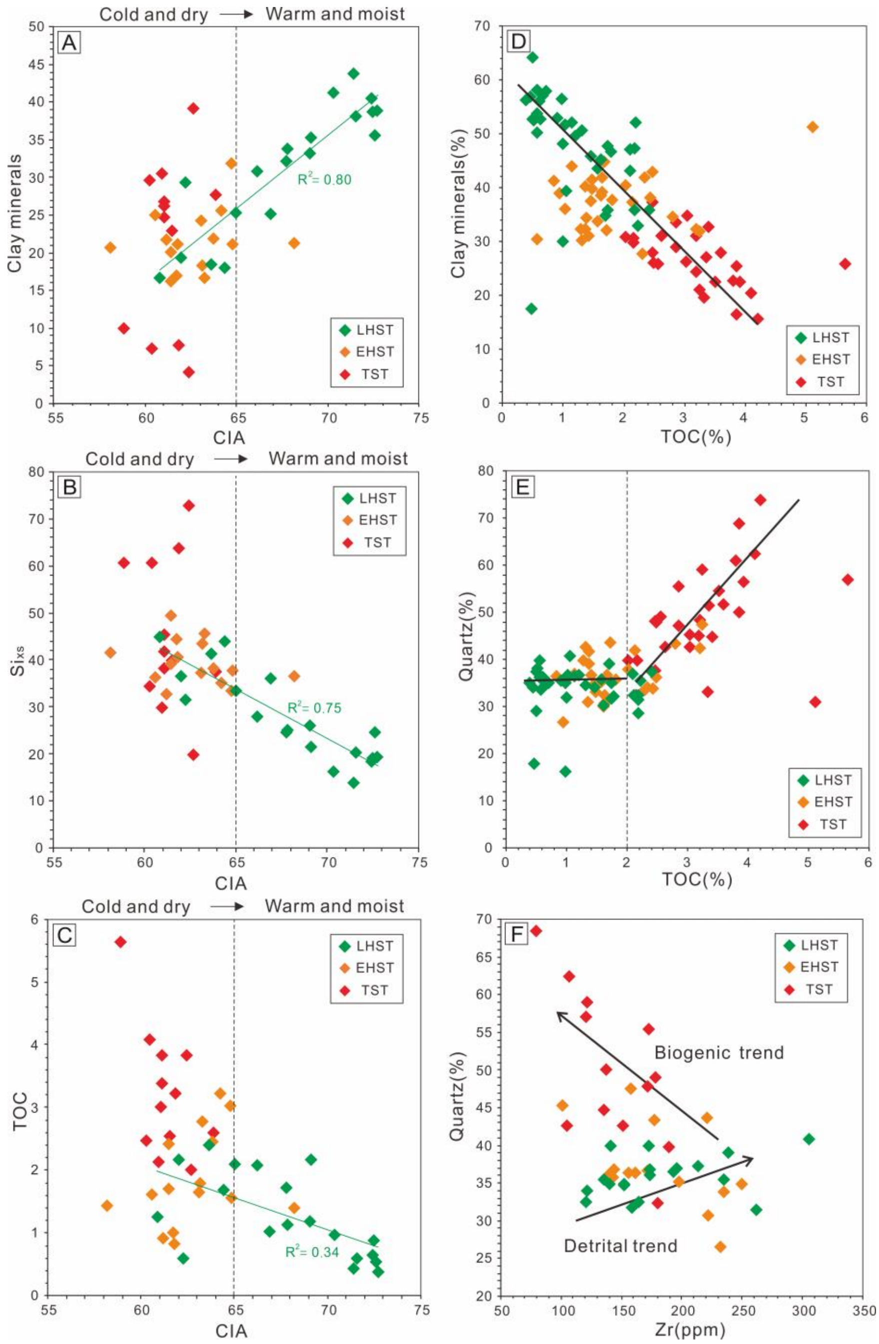

Figure 12. Climate change form Wufeng Formation to Longmaxi Formation triggers minerals and organic matter in differential input at different systems tracts.

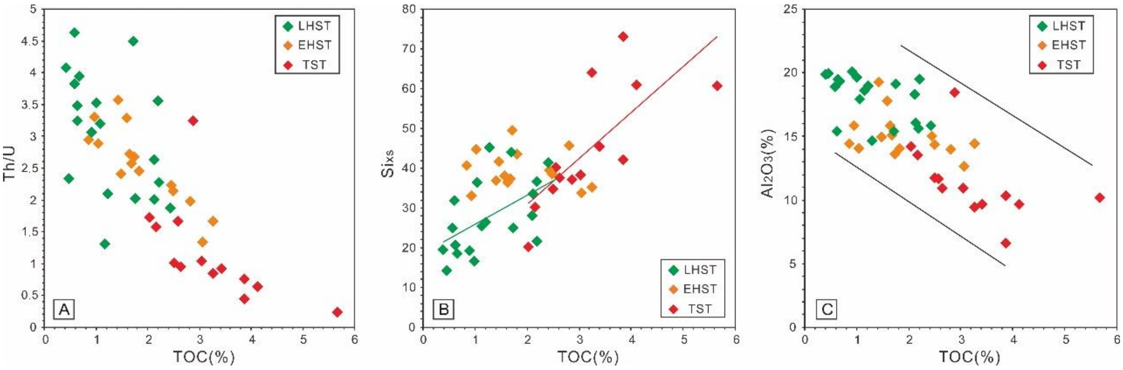

Figure 13. The relationships of TOC content to Th/U, Si_{xs} and Al_2O_3 in different systems tracts of Wufeng-Longmaxi formation in Jiaoshiba area.

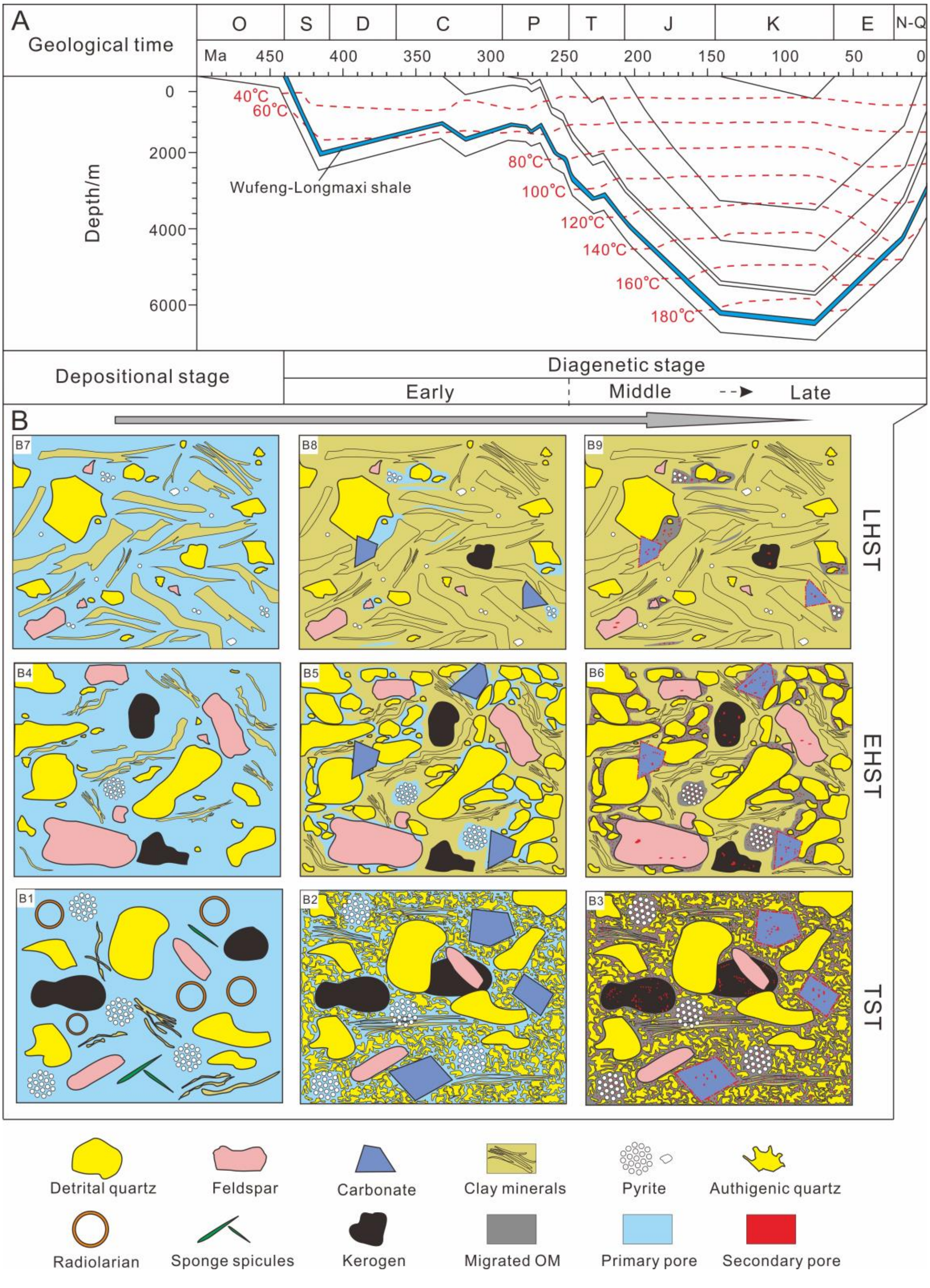

Figure 14. (A) Burial history of Wufeng-Longmaxi shale (modified from Guo et al., 2016). (B) A conceptual model of the depositional and diagenetic process of shales in different systems tracts.

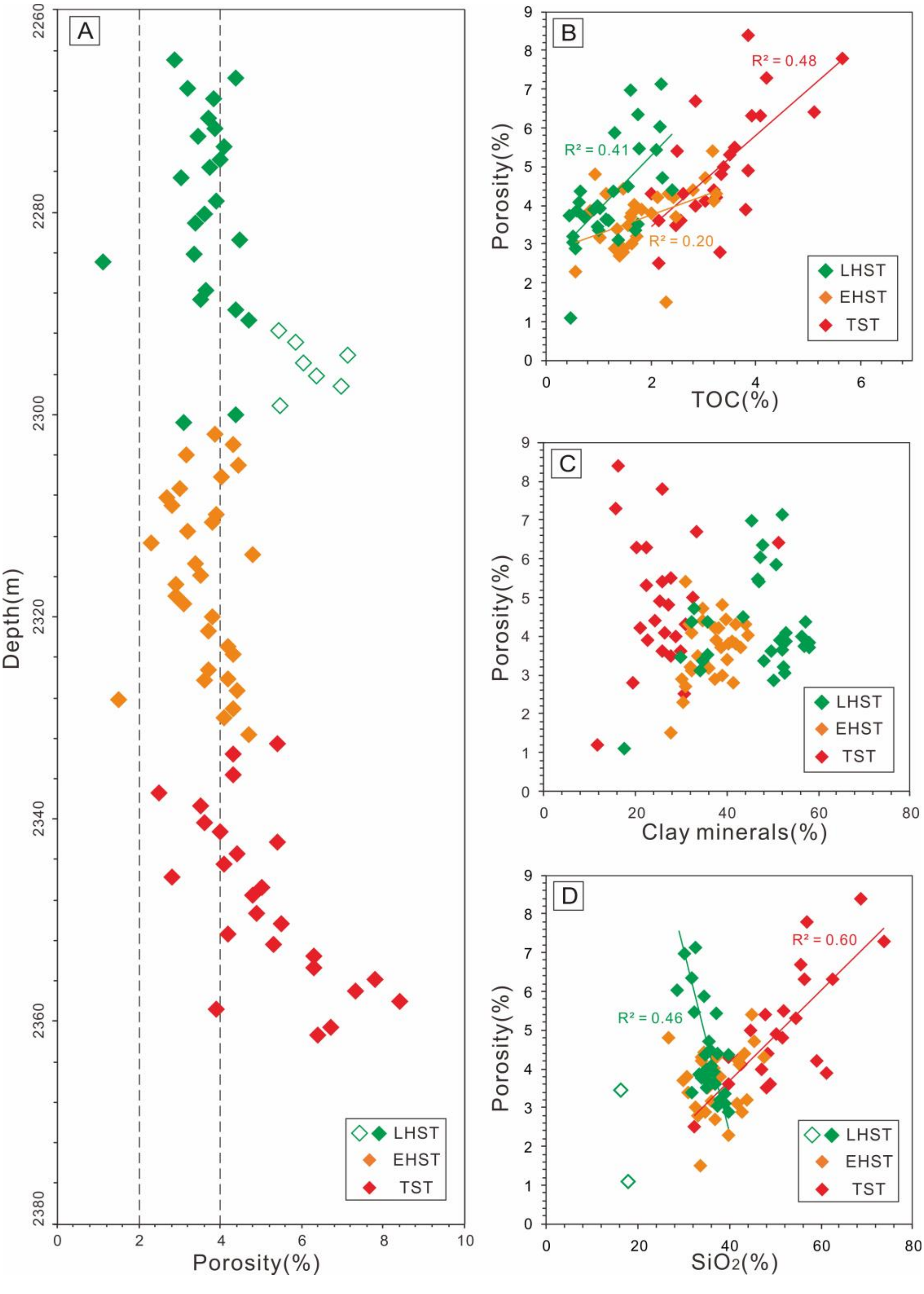

Figure 15. Porosity variation and its relationship of TOC, clay mineral and quartz content of samples in Well A.

Table 1. Pore characteristics of samples in Wufeng-Longmaxi Formation obtained by Nano-CT analysis.

Sample	Sequence	Data-Body volume	Total OM Volume	Total Pore Volume	Pore Number	Porosity	TOC
		μm^3	μm^3	μm^3		(wt.%)	(wt.%)
X1	TST	16662.26	1097.68	472.68	101	2.84	6.59
X2	EHST	16662.26	666.08	444.03	1411	2.66	4
X3	LHST	16662.26	688.02	377.47	2251	2.26	4.13